USGS
science for a changing world

Prepared in cooperation with the New Mexico Environment Department

Questa Baseline and Premining Ground-Water Quality Investigation 18. Characterization of Brittle Structures in the Questa Caldera and Their Potential Influence on Bedrock Ground-Water Flow, Red River Valley, New Mexico

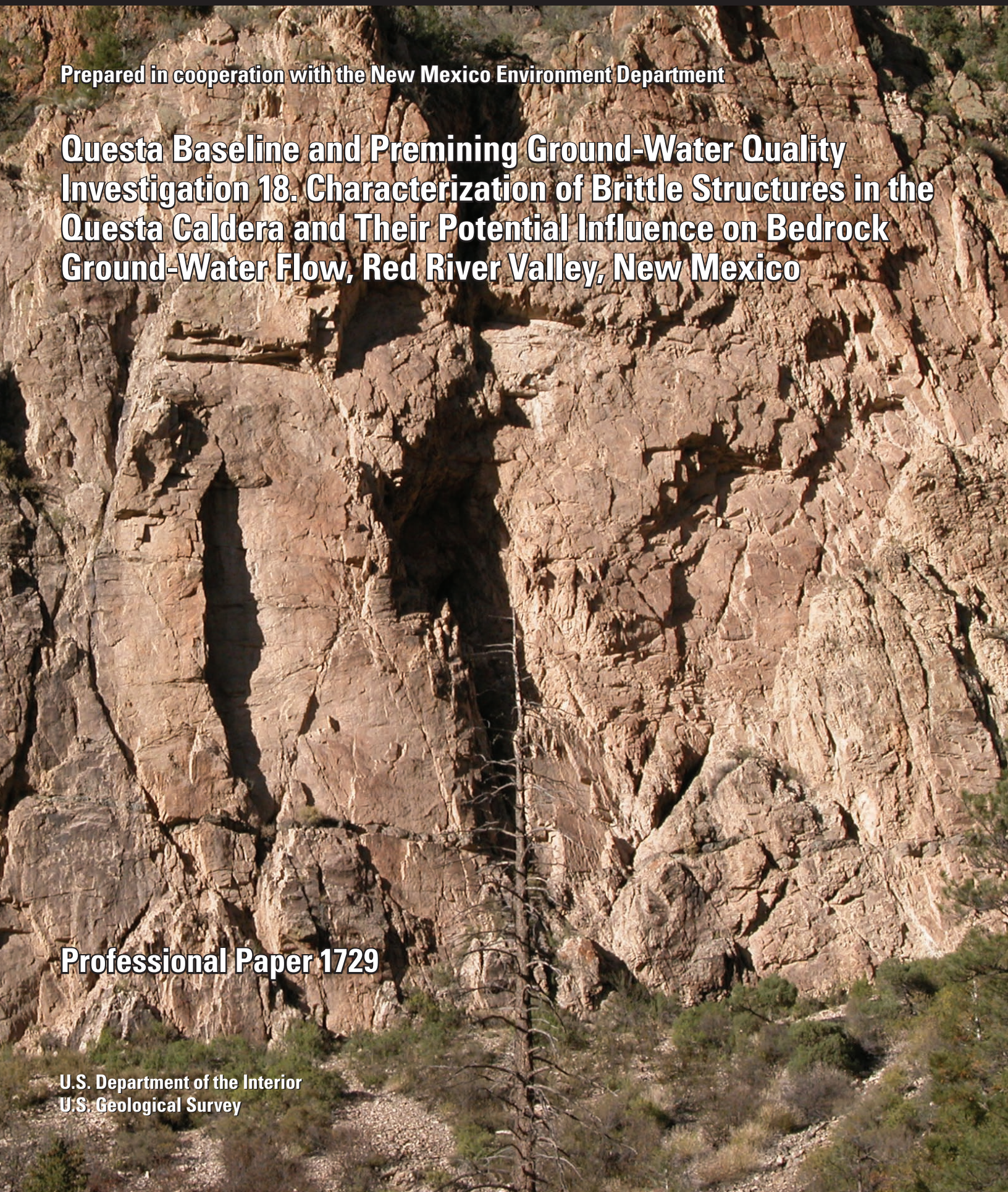

Professional Paper 1729

U.S. Department of the Interior
U.S. Geological Survey

Questa Baseline and Premining Ground-Water Quality Investigation 18. Characterization of Brittle Structures in the Questa Caldera and Their Potential Influence on Bedrock Ground-Water Flow, Red River Valley, New Mexico

By Jonathan Saul Caine

Prepared in cooperation with the New Mexico Environment Department

Professional Paper 1729

U.S. Department of the Interior
U.S. Geological Survey

U.S. Department of the Interior
DIRK KEMPTHORNE, Secretary

U.S. Geological Survey
Mark D. Myers, Director

U.S. Geological Survey, Reston, Virginia: 2006

For product and ordering information:
World Wide Web: http://www.usgs.gov/pubprod
Telephone: 1-888-ASK-USGS

For more information on the USGS--the Federal source for science about the Earth, its natural and living resources, natural hazards, and the environment:
World Wide Web: http://www.usgs.gov
Telephone: 1-888-ASK-USGS

Suggested citation:
Caine, Jonathan Saul, 2006, Questa baseline and premining ground-water quality investigation 18. Characterization of brittle structures in the Questa caldera and their potential influence on bedrock ground-water flow, Red River Valley, New Mexico: U.S. Geological Survey Professional Paper 1729, 37 p.

Contents

Figures

Tables

Questa Baseline and Premining Ground-Water Quality Investigation 18. Characterization of Brittle Structures in the Questa Caldera and Their Potential Influence on Bedrock Ground-Water Flow, Red River Valley, New Mexico

By Jonathan Saul Caine

Abstract

This report presents a field-based characterization of fractured and faulted crystalline bedrock in the southern portion of the Questa caldera and its margin. The focus is (1) the identification and description of brittle geological structures and (2) speculation on the potential effects and controls that these structures might have on the potential fluxes of paleo to present-day ground water in relation to natural or mining-related metal and acid loads to surface and ground water. The entire study area is pervasively jointed with a few distinctive patterns such as orthogonal, oblique orthogonal, and conjugate joint sets. Joint intensity, the number of joints measured per unit line length, is high to extreme. Three types of fault zones are present that include partially silicified, low- and high-angle faults with well-developed damage zones and clay-rich cores and high-angle, unsilicified open faults. Conceptually, the joint networks can be thought of as providing the background porosity and permeability structure of the bedrock aquifer system. This background is cut by discrete entities such as the faults with clay-rich cores and open faults that may act as important hydrologic heterogeneities. The southern caldera margin runs parallel to the course of the Red River Valley, whose incision has left an extreme topographic gradient at high angles to the river. Many of the faults and fault intersections run parallel to this assumed hydraulic gradient; thus, these structures have great potential to provide paleo and present-day, discrete and anisotropic pathways for solute transport within the otherwise relatively low porosity and permeability bedrock background aquifer system. Although brittle fracture networks and faults are pervasive and complex, simple Darcy calculations are used to estimate the hydraulic conductivity and potential ground-water discharges of the bedrock aquifer, caldera margin, and other faults in order to gain insight into the potential contributions of these features to the ground-water and surface-water flow systems. These calculations show that, because all of these features are found along the Red River in the Cabin Springs–Columbine Park–Goat Hill fan area, their combined effect increases the probability that the bedrock aquifer ground-water flow system provides discharge to the Red River along this reach.

Introduction

The Questa caldera is exceptionally well exposed in the Red River Valley of northern New Mexico and is host to important metallic mineral deposits, particularly molybdenite (fig. 1). These deposits, mined since the late nineteenth century, are associated with extensive and noneconomic hydrothermal alteration and pyritization of the country rock. Both natural and mining-related trace-metal and acid loading to surface and ground water occurs in the Red River Valley. The overall purpose of this multireport, baseline investigation is to characterize the geological, hydrological, and geochemical attributes of the Red River Valley that control the premining ground-water quality. The purpose of this particular report is the characterization of the crystalline bedrock aquifer in the Red River Valley where the occurrence, storage, and flow of ground water, the solutes within it, and its interactions with surface water and the Molycorp molybdenite mine are largely controlled by fracture networks and fault zones. This report also complements other U.S. Geological Survey (USGS) reports on the geological, geochemical, geophysical, and hydrological characteristics of the lower Red River watershed (Lucius and others, 2001; Livo and Clark, 2002; Briggs and others, 2003; Caine, 2003; McCleskey and others, 2003; Powers and Burton, 2003; LoVetre and others, 2004; Ludington and others, 2004; Naus and others, 2005; and Nordstrom and others, 2005).

Field-based study of fracture networks and fault zones in crystalline bedrock helps to characterize the potential physical heterogeneities that may control the bedrock ground-water

flow system. The southern margin of the Questa caldera provides a unique opportunity to complete such a study in a deeply eroded, mineralized, and hydrothermally altered caldera margin setting (figs. 1 and 2).

The Questa caldera is a complex hydrogeologic system containing four major, generic, hydrogeologic units of concern. These include, in order of inferred decreasing bulk porosity and permeability: (1) waste-rock piles associated with mining operations, (2) surficial materials such as Quaternary and Holocene sediments, (3) weathered bedrock, and (4) relatively unweathered bedrock. All of the bedrock in the study area is either crystalline intrusive, extrusive, or metamorphic rock (Lipman, 1983; Lipman and Reed, 1989). The primary unweathered or hydrothermally altered intergranular porosity and permeability of the rocks are low compared to many sedimentary rocks (for example, see Freeze and Cherry, 1979). The porosity and permeability of the Questa bedrock are fundamentally controlled by secondary brittle structures such as joints, faults, and fault zones. Mineralization in the form of veins and hydrothermal alteration zones and the depth of weathering of these brittle structures and hydrothermal alteration zones also affect the porosity and permeability structure of the bedrock, probably to diminishing degrees with depth (for example, Ludington and others, 2004). Understanding the occurrence, storage, and flow of ground water in the bedrock as controlled by secondary porosity and permeability, as well as their heterogeneity, is predicated on understanding the types and geometric extents of brittle structures in the study area. Rock units exposed in the study area represent a deeply eroded portion of the Questa caldera system (see Lipman, 1983). Therefore, the extent to which the structures described here, and their potential hydrogeological effects, are representative of calderas in general is unknown.

Physical Setting

Geographic and Physiographic Features

The study area is located in Taos County in the Taos Range of the Sangre de Cristo Mountains of north-central New Mexico (fig. 1). The Red River drainage basin is a tributary to the Rio Grande within the Carson National Forest. The area is a rugged, mineralized, and hydrothermally altered terrain with steep slopes and V-shaped valleys (fig. 1). The study reach of the Red River is in the Red River Valley between the gaging station at 2,280-m elevation at the west end and the town of Red River at 2,646-m elevation at the east end (fig. 1). The canyon walls of the Red River Valley rise steeply from 2,400 m to over 3,000 m at the ridge crest on both the north and south sides of the river. Some peaks reach nearly 3,500 m. The 600-m difference in elevation between the Red River and the adjacent ridge crest can occur over a horizontal distance of less than 2,000 m.

The Molycorp, Inc., Questa Molybdenite mine, referred to as the mine site, is located on the north side of New Mexico State Highway 38 and the Red River 13 km east of the mountain front and the mouth of the Red River canyon. The mine site is approximately 16 km^2 and encompasses three main tributary valleys to the Red River: Capulin Canyon, Goat Hill Gulch, and Sulphur Gulch, from west to east, respectively (fig. 1).

Mining activities produced extensive underground workings and an open pit of approximately 0.65 km^2 near or in Sulphur Gulch. Waste-rock piles cover steep slopes on the north side of the Red River between Capulin Canyon and Spring Gulch (a tributary valley of Sulphur Gulch). Hydrothermally altered bedrock is present in Capulin, Goat Hill, Sulphur, Hansen, Straight, June Bug, Hottentot, and Bitter Creek drainages (fig. 1). The latter five drainages are examples of unmined drainages with the exception of minor prospects in Bitter Creek. Weathering of extensively altered rock has resulted in steep, highly erosive, sparsely vegetated “alteration scars” that are clearly visible from the ground and in aerial photographs (Meyer and Leonardson, 1990). Where there has been no mining, these scar areas also are important natural sources of trace-metal and acid loading to surface and ground waters.

Climate and Vegetation

The Red River Valley lies within a semiarid desert that receives precipitation throughout the year and sustains moderate biodiversity. Between 1915 and 2002, the annual average temperature was 4°C, the precipitation and snowfall were 52 cm and 370 cm, respectively, and the daily temperatures generally fluctuated by 18°C throughout the year (Western Regional Climate Center, 2003).

Climate and vegetation vary greatly within short distances because of differences in topography, weather, bedrock, and sediment composition. Orographic effects of mountainous topography lead to precipitation on the windward slopes and localized storms within tributary valleys. Major precipitation events include summer thunderstorms and winter/spring snowstorms. Thunderstorms are responsible for mass wasting in hydrothermally altered scar areas, producing debris flows that may affect vegetation, alluvial aquifers, and the Red River. Winter snowpack contributes to ground-water recharge through snowmelt infiltration and runoff.

Prevalent vegetation in the Red River Valley is representative of the following altitude zones: piñon-juniper woodland (1,800–2,300 m), mixed conifer woodland (2,300–2,740 m), and spruce-fir woodland (2,740–3,660 m; Knight, 1990). Willows, cottonwoods, shrubs, perennial grasses, and flowering vegetation are common near the banks of the Red River. Extending from the river are widely spaced piñon pines and junipers. Gains in altitude first give rise to an abundance of ponderosa and limber pines and to Douglas and white fir at higher altitudes. This typical mountain community, although diverse, is dominated by ponderosa pines (Larry Gough, U.S. Geological Survey, oral commun., 2003).

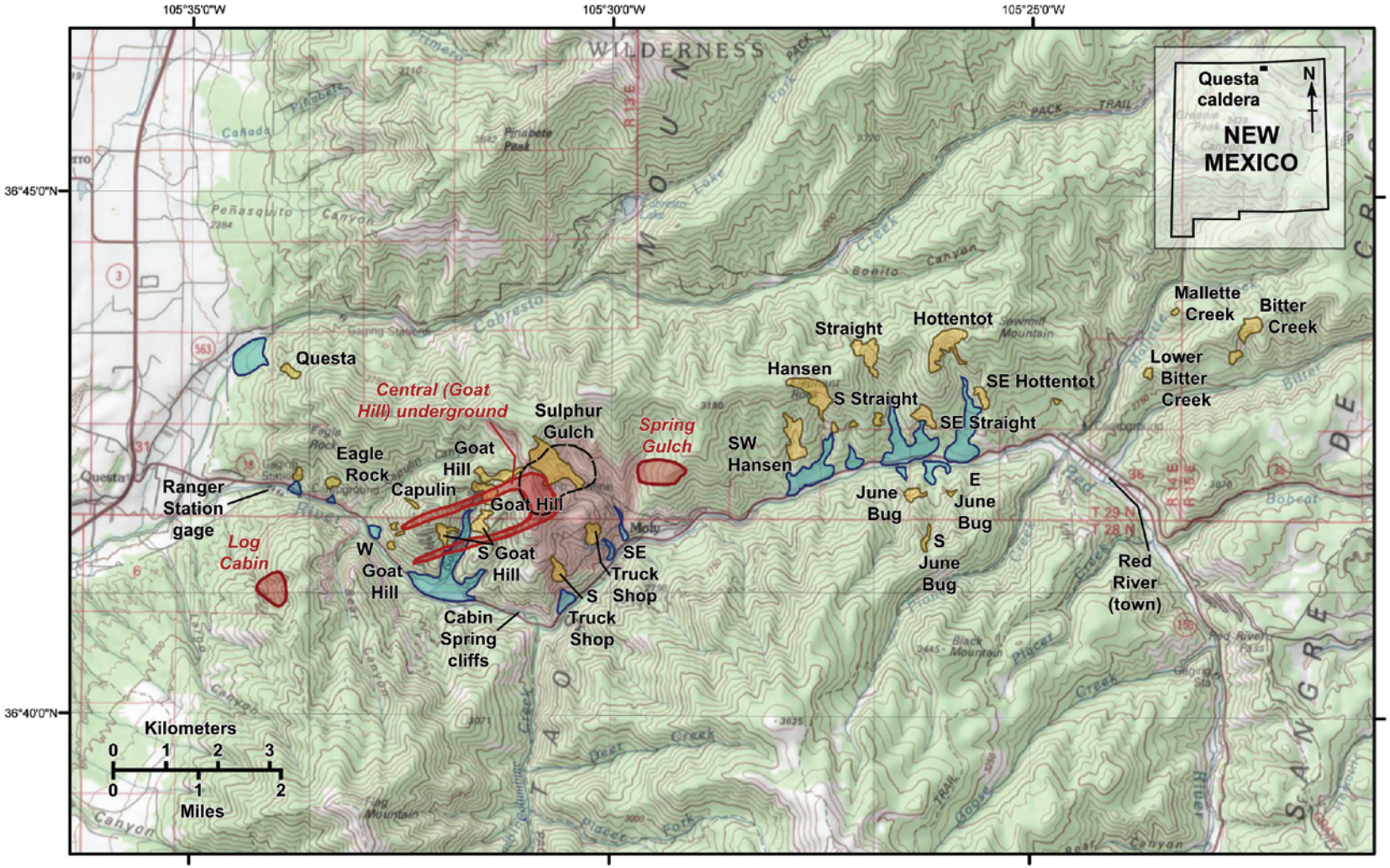

Figure 1. Location and topographic map of the study area, showing alteration scars (yellow), debris fans (blue), known ore bodies (red), the mine site (pink), and the open pit (black dashed line). Topography from U.S. Geological Survey, 1:100,000 Wheeler Peak 30 × 60 quadrangle. Scar geology courtesy of Geoff Plumlee.

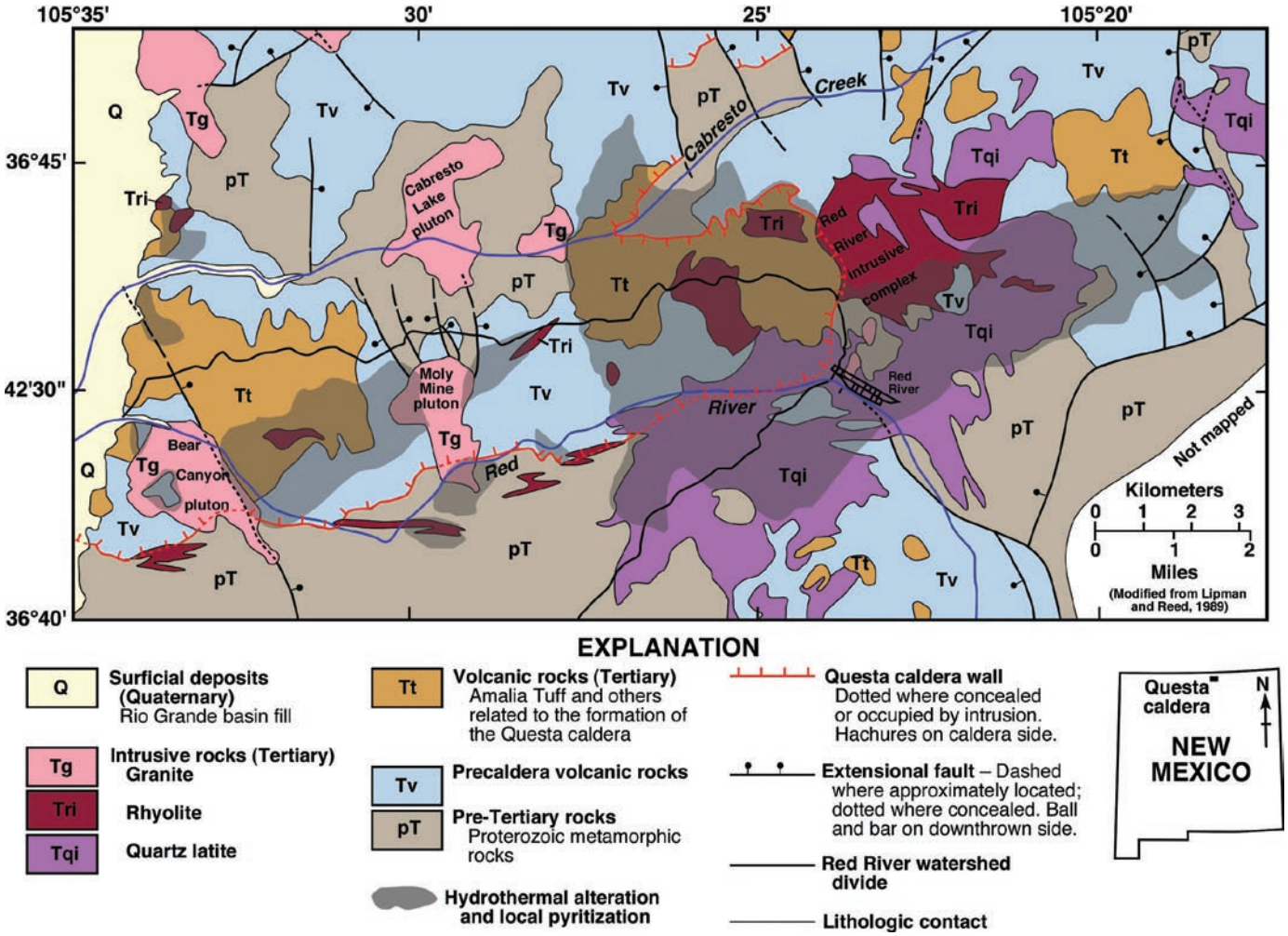

Figure 2. Simplified geologic map of the southern portion of the Questa caldera in the vicinity of Red River, New Mexico, modified from Lipman and Reed, 1989. The individual rock types shown are a starting point for conceptualizing what might be hydrologically significant units or domains in the study area and were used as a guide for collecting brittle-structures data. Note that the areas affected by hydrothermal alteration are shaded in transparent gray.

General Geology

The geochemical interaction of water with soil, colluvium, alluvium, and fractured bedrock produces the composition of surface and ground waters that are the overall focus of this baseline and premining ground-water-quality investigation. Hence, the geology is a fundamental component to understanding the hydrology and ground-water chemistry. This section briefly summarizes the general geologic framework from Schilling (1956), Rehrig (1969), Lipman (1981), and Meyer and Leonardson (1990, 1997), in addition to observations made by the USGS scientists currently working at the site (Ludington and others, 2004).

The Taos Range is composed of Precambrian metamorphic rocks and granitic intrusive rocks overlain and intruded by Tertiary volcanic and plutonic rocks (fig. 2). The volcanics are primarily of intermediate to felsic composition (andesites to rhyolites) and are intruded by late Oligocene and early Miocene quartz monzonites and granites that provided the source of the hydrothermal fluids and molybdenite mineralization. The hydrothermally altered volcanics commonly contain pyrite mineralization (generally 1–3 percent). The Red River Valley lies along the southern edge of the Questa volcanic caldera and contains complex structural features and extensive hydrothermal alteration associated with the evolution of the Rio Grande rift (figs. 1 and 2). The mineral deposits in the Red River Valley are considered Climax-type deposits that are associated with silica- and fluorine-rich rhyolite porphyry and granitic intrusives. The three principal alteration zones include highly altered quartz-sericite-pyrite (QSP), less-altered argillic (dominantly kaolinite) zones, and mildly altered propylitic zones (containing calcite mineralization). Quartz-sericite-pyrite alteration, as the name implies, produces a mixture of quartz, pyrite (up to 10 percent), and fine-grained mica

(sericite) or illite. Chlorite, epidote, albite, and calcite typically are present in the propylitic assemblages. Ore deposits contain quartz, molybdenite, pyrite, fluorite, calcite, manganiferous calcite, dolomite, and rhodochrosite. Lesser amounts of galena, sphalerite, chalcopyrite, magnetite, and hematite also are present. The hydrothermal alteration related to mineralization overprints an older, regional propylitic alteration. In these altered areas, rocks can contain a mixture of quartz, pyrite, and illite clays replacing feldspars, chlorite, carbonates, and epidote. Abundant minerals in waste rock produced by mining activities include chlorite, gypsum, illite, illite-smectite, jarosite, kaolinite, and muscovite (Gale and Thompson, 2001).

Andesite volcanic and volcaniclastic rocks are present in most scar-area bedrock outcrops and are the dominant bedrock units in the Straight Creek, South and Southeast Straight Creek, South Goat Hill, Sulphur Gulch, and Southwest Hansen scars (Ludington and others, 2004, and fig. 1). Amalia Tuff, a mildly alkaline, rhyolitic tuff, is the dominant rock type in the Goat Hill and Hansen scars, and quartz latite porphyry is the main rock type in the June Bug and Southeast Hottentot scars (fig. 1). Rhyolite porphyry is the main rock type in the Hottentot scar, and quartz latite and rhyolite porphyries form the hillslopes of many scars. Rhyolite porphyry and tuff do not seem to have been substantially affected by propylitization. Advanced argillic alteration was identified in the Hansen and Hottentot scars and in areas southwest of the Molycorp open pit. Propylitized andesite bedrock is present in several drainages that typically do not contain alteration scars.

After eruption of the Amalia Tuff and the formation of the Rio Grande rift 26 million years ago, the landscape of the study area consisted of a broad, low-relief plateau (P.W. Lipman, written commun., 2005). Rifting has caused as much as 7 km of structural relief across the Sangre de Cristo fault system that forms the eastern structural boundary of the rift and the western boundary of the Sangre de Cristo mountain block (Kluth and Schaftenaar, 1994; Grauch and Keller, 2004). Tectonically driven uplift caused the Red River to incise into the Taos Range resulting in the development of today's rugged terrain (Kirk Vincent, U.S. Geological Survey, written commun., 2005). However, prior to a million years ago, the Red River was essentially the headwater of the Rio Grande and it flowed near the level of the top of the sediments within the rift basin (Wells and others, 1987). About 700 to 600 thousand years ago the San Luis Basin was captured by the Rio Grande, notably increasing discharges and incision in the Rio Grande and tributary watersheds and relegating the Red River to the status of one of those tributaries (Wells and others, 1987). Although thin Pleistocene alpine glaciers formed in the highest peaks of the Sangre de Cristo Mountains, they probably had little influence on the form of the Red River Valley.

During the late Holocene, forested hillslopes eroded at about 0.04 mm/yr as compared to the then-exposed alteration scars, which eroded at about 3.0 mm/yr (Kirk Vincent, written commun., 2005). This extremely rapid erosion rate caused tributary watersheds containing alteration scars to deliver more sediment to the Red River than it could transport away, thus developing large debris fans to interfinger with alluvial sediments within the valley (Kirk Vincent, written commun., 2005). These hydrothermally and structurally controlled facies relationships have resulted in significant heterogeneities within the generally high permeability Red River Valley alluvial aquifer because the fan deposits have several orders of magnitude lower permeability than the alluvial deposits.

Tectonic deformation combined with igneous and exhumation processes from Precambrian through Holocene times have produced a highly complex array of folds, fault zones, fractures, and veins. Since the inception of the caldera in the Oligocene, the region around the Red River Valley has been in a tensional stress regime that has ultimately produced the ancient and modern Rio Grande rift as previously discussed (Meyer and Foland, 1991; figs. 1 and 2). Generally north-northwest- to north-northeast-striking extensional fault zones have been progressively reactivated during the coupled development of the caldera, the ore mineral system, and the eastern rift flank. These fault zones have accommodated approximately 200 percent extensional strain focused in the caldera (Meyer and Foland, 1991; fig. 2) and show a wide variety of internal deformation and structures, degree of mineralization, and dip. Numerous fracture networks, joints, and veins pervasively penetrate the entire study area. Collectively, these brittle structures form the permeability structure, in otherwise generally low permeability crystalline rock, in which the modern geochemical and ground-water flow system exists.

Bedrock at the surface and buried under alluvial, colluvial, and anthropogenic deposits shows a variable and complex zone of weathering. Samples collected from a weathering profile in the Straight Creek scar were studied in detail to characterize the mineralogic variations in a weathered profile (see Ludington and others, 2004, and fig. 1). Relatively unweathered bedrock exposed in the creek bottom is propylitized andesite with a QSP overprint. Depending on location within the weathering profile, altered rocks contain variable amounts of quartz, illite, chlorite, and plagioclase feldspar, with smaller amounts of pyrite, gypsum, rutile, jarosite, and goethite (Livo and Clark, 2002; Ludington and others, 2004). Calcite, goethite, and sericite are widely distributed in the Red River Valley rocks and soils, as revealed by Airborne Visible/Infra-Red Imaging Spectrometer data (AVIRIS) (Livo and Clark, 2002). Calcite is an important mineral in the Red River Valley because its dissolution effectively neutralizes the acid inflows so that pH values in the Red River tend to be alkaline (pH 7–8). Gypsum is common throughout the Red River Valley and forms as a secondary product of acid-sulfate weathering when pyrite oxidizes and reacts with calcite. Because gypsum is soluble in water, calcium and sulfate are the major ions in most surface and ground waters in the Red River Valley.

The major minerals in rock samples collected during mineral exploration and mining are biotite, calcite, chalcopyrite, fluorite, galena, molybdenite, pyrite, quartz, rhodochrosite, and sphalerite. Mining activities produced roughly 328 million tons of rock overburden in Capulin Canyon, along the north slope of the Red River, and in Goat Hill and Sulphur and Spring Gulches (URS,

written commun., 2001). The abundant minerals in waste-rock samples include chlorite, gypsum, illite, illite-smectite, jarosite, kaolinite, and muscovite (Gale and Thompson, 2001).

Mining History

Prior to 1916, prospectors discovered outcrops of rich, yellow, weathered rock that looked like sulfur (hence the name, Sulphur Gulch) and a greasy mineral that looked like graphite (fig. 1). The graphitic mineral was identified as molybdenite in 1916, and the yellow mineral was ferrimolybdite, the oxidized product derived from the weathering of molybdenite (Schilling, 1956). By 1920 the Molybdenum Corporation of America had acquired the property to mine the deposit, and the company subsequently shortened its name to Molycorp, Inc. A mill and flotation plant was set up by 1923, and small-scale underground mining of high-grade veins (averaging 4 percent with a maximum of 35 percent) continued until 1958. During the 1950s exploration identified a large, low-grade deposit (about 0.3 percent) below the high-grade deposit, and the decision was made to extract this ore by open-pit methods (Carpenter, 1968). Extraction of open-pit ore began in 1965, and tailings were transported by a 9-mile-long pipeline to a tailings facility in the Rio Grande Valley just west of Questa. Peak annual production of 11.5 million pounds occurred in 1976. In 1977 Molycorp, Inc., became a wholly-owned subsidiary of Union Oil Company of California.

Open-pit mining ceased in 1983 and underground mining restarted. Waste rock was no longer dumped onto piles at the mine site, but the volume of tailings transported in the pipeline to the Questa facility increased. Low market values for molybdenum have periodically caused the mine to shut down (1986–89 and 1992–95). Active mining continues at Molycorp's Questa mine in response to market demand. Further history and related information on the Questa Molycorp mine are available from Molycorp, Inc. (www.molycorp.com) and from the U.S. Environmental Protection Agency (www.epa.gov/superfund/sites/npl/nar1599.htm).

General Hydrology

Surface Water

The Red River originates at an altitude of approximately 3,658 m near Wheeler Peak, the highest peak in New Mexico (4,011 m), and flows roughly 55 km to its confluence with the Rio Grande at an altitude of 2,012 m. Total basin drainage area is 492 km^2, and the drainage area upstream from the Questa Ranger Station gaging station (at the mouth of the Red River Canyon) is 293 km^2 (fig. 1). Peak streamflow usually occurs from late May to mid-June, with snowmelt-related flows beginning in late March and increasing through mid-April. Summer thunderstorms are common in July and August. Between 1930 and 2001, the mean annual discharge of the Red River at the Questa Ranger Station gage has ranged from 0.36 to 2.92 m^3/s, and the average daily discharge ranged from 0.07 to 21.24 m^3/s with an average of 1.33 m^3/s (U.S. Geological Survey, 2004).

The main drainages in the vicinity of the mine site are Capulin Canyon, Goat Hill Gulch, and Sulphur Gulch on the north side of the Red River (fig. 1). Upstream from the mine site, Hansen, Southwest Hansen, Straight, Hottentot, and Bitter Creeks drain scar areas, whereas Mallette Creek drains a nonscar area on the north side of the Red River. Bear Canyon, Columbine, Pioneer, and Placer Creeks drain largely unmineralized land on the south side of the river (fig. 1). Bear Canyon and upper Pioneer Creeks also contain some mineralization. Downstream from the mine site and in the Rio Grande Rift Valley, the Red River joins with Cabresto Creek, which enters from the north, before it discharges to the Rio Grande.

Springs and shallow alluvial ground water discharge to the Red River, rendering it a gaining stream over much of its length (Smolka and Tague, 1989). Between the town of Red River and the gaging station near Questa, there are about 25 ephemeral seeps and springs along the banks of the Red River and approximately 20 intermittent seeps and springs in tributary drainages on the north side of the river (South Pass Resources, Inc., written commun., 1995; Steffen, Robertson, & Kirsten, written commun., 1995; Robertson GeoConsultants, Inc., written commun., 2001). Most seeps and springs are acidic (pH 2–4) with high conductance, dissolved solids, and metal concentrations. Aluminum hydroxide often precipitates from springs downgradient from scar and mined areas on the north side of the Red River, affecting the color and turbidity of the river (Vail Engineering, Inc., 1989).

Ground Water and Aqueous Geochemistry

Aquifer and other geologic and anthropogenic units in the Red River Valley are highly varied. Waste-rock piles and scars with associated debris fans are geochemically reactive, have high porosity, and have relatively high permeability. Some of the permeability may form from transient desiccation processes, episodic mass movements, or creep that form irregular and fracturelike openings at a wide range of scales in these poorly consolidated surficial materials. Alluvial aquifers are restricted in areal extent and have variable compositions. Hillslope soils are thin and composed of materials eroded from adjacent upgradient slopes. Debris fans are composed of sediments rapidly shed from their respective watersheds. Where the tributary watersheds contain "alteration scars," the debris fans are large and active and contain both coarse and fine-grained, largely unsorted, clay-rich, debris-flow sediments, making them heterogeneities in the alluvium, as previously discussed.

The chemistry of these sediments reflects the chemistry of their source terrains. The rapidly eroding and altered erosion scars have source materials that can generate low-pH,

trace-metal-rich ground water. Sediments deposited by the Red River, in contrast, generally consist of well-washed, rounded sands, gravels, and cobbles and are composed of a mix of lithologies present in the entire Red River basin, including carbonates from the uppermost reaches. The largest debris fans caused the Red River alluvium to aggrade behind the fans during the Quaternary. Thus, ground water flowing in the shallow alluvial aquifer passes alternately through Red River alluvium and debris fans and may emerge when a relatively low permeability fan is contacted. Both the Red River alluvium and debris fans as a complex aquifer unit are less than several hundred meters wide and less than 100 m thick.

Alluvial ground water is a calcium-sulfate water type with magnesium commonly the second most abundant cation. Ground water downgradient from the waste-rock dumps and scars has acidic pH values and elevated metal concentrations compared to ground water upgradient from these altered areas.

The bedrock aquifer constitutes the largest mass of aquifer in the study area but probably contains only relatively small amounts of ground water below the weathered zone because of inferred low porosity and low permeability largely controlled by fracture networks. Bedrock ground waters are also calcium-sulfate type but usually of neutral pH. Most wells developed in the Red River Valley were installed to monitor water quality downgradient from mining operations (waste-rock dumps and tailings piles) and(or) scar areas. Wells installed in the Straight Creek drainage (fig. 1) during this study were developed for the purpose of measuring water levels and collecting water-chemistry samples for a range of environments in the Red River Valley, similar to the mine environment, and to interpret the water/rock interactions under nonmining baseline conditions as a reference for premining water/rock interactions for the mine site.

Hydrothermal alteration produced substantial changes in mineralogy over relatively short distances, a common feature of hydrothermally altered terrains. Hence, both the mineralogy and the resultant water chemistry can change substantially on a small spatial scale. Such hydrogeochemical environments are described as highly heterogeneous, making the estimation of premining ground-water chemistry a highly variable function of changing lithology rather than single fixed concentrations for an area the size of the mine site.

Methods and Previous Work

Field data including outcrop scale measurements and observations and descriptions of geological structures and host lithology were collected from representative outcrops of each of the major bedrock lithologic groups in the study area (see Caine, 2003). These data characterize brittle structures and document the major potential structural heterogeneities that may impart potential anisotropy, or possible fast pathways and preferential flow paths, for the transport of contaminants from the bedrock to surficial deposits or water bodies such as the Red River. Specific data collected in this study include fault zone, caldera margin, lithologic contact, and fracture network geologic and geometric properties such as orientation, composition, mineralization and alteration, intensity, length, shear sense and relative age, width, and shape. Numerous rock samples were collected (see Caine, 2003, for the computer file of the raw data). Explanations of the methods used in this characterization are provided in Caine and others (1996), Caine (2001a, b, c), Caine (2003), and Caine and Tomusiak (2003). Site-specific hydraulic data, tracer studies, aquifer pumping tests, borehole geophysical logging, and thermal and geochemical measurements should be conducted to verify the field data and associated interpretations.

Previous work by Carpenter (1968), Rehrig (1969), Lipman (1983), Lipman and Reed (1989), and Meyer and Foland (1991) has established the foundation of the exceptionally complex bedrock geology of the study area. Meyer and Leonardson (1997) have added to this foundation through highly detailed outcrop-scale mapping at 1:6,000, the identification of numerous brittle structures, and a description of the geologic history and processes they represent. Several unpublished consultant reports also have contributed to understanding the bedrock hydrogeologic system. This report is the first known outcrop-scale characterization of brittle structures in bedrock in the specific context of their potential effects on the paleo to present-day ground-water flow system of the Questa caldera.

For the purpose of characterization of brittle structures, the bedrock geology can be broken into several significant rock groups that may have unique brittle structural attributes and that also might make those rock groups significant hydrogeological and hydrogeochemical units (see fig. 2, ensuing descriptions, and Ludington and others [2004], for a detailed description of the geology of the study area). These units include (1) Precambrian quartzo-feldspathic metamorphic rocks, (2) Tertiary precaldera volcanic rocks that are dominantly andesitic flows, (3) Tertiary Amalia Tuff, (4) Tertiary quartz latite flows, (5) Tertiary megabreccias, (6) Tertiary rhyolite intrusives, (7) Tertiary granitic intrusive rocks, (8) Tertiary siliciclastic sediments, and (9) numerous types of surficial deposits that were not studied as part of the bedrock characterization (Ludington and others, 2004). Structural and lithological data were collected from representative outcrops of each of these rock groups except the quartz latite flows to provide a the foundation for understanding the potential effects on the ground-water flow system.

On the basis of reported mass-balance calculations, an unaccounted-for ground-water discharge was identified along the Cabin Springs reach of the Red River, near an intersection of the caldera margin with the Red River (Kirk Vincent, written commun., 2005). To evaluate whether or not this discharge could come from the bedrock alone, from the caldera margin, from one or more of the fault zones, or from some combination of these, a set of simple Darcy calculations was performed, and the results are presented in this report. Using measured potential hydraulic gradients and cross-sectional areas and the unaccounted-for discharge values, theoretical values of hydraulic conductivities were calculated and compared with values reported from aquifer

tests from bedrock in the Questa mine area. Theoretical hydraulic conductivity values for the caldera margin, faults, and fault zones were compared with numerical model results for modeled fault zones as reported in the literature. This set of calculations, although oversimplified, demonstrates that either the bedrock alone, the caldera margin, an individual and narrow open extensional fault, or some combination of these, could produce the unaccounted-for discharge. These results illustrate the important point that often no unique solutions exist when making links between geological inference and hydraulic reality, particularly in highly complex geological environments. However, these results provide a starting point in setting up testable hypotheses that illustrate what the most important physical conditions and heterogeneities might be, regarding the interactions of mass flux from bedrock to surficial deposit aquifers, to the open pit and underground mine workings.

Brittle Structures of the Questa Caldera

Joint Networks

Joints are fractures whose primary direction of opening is perpendicular to their walls and that are not filled with mineral precipitates. Fractures filled with mineral precipitates will be referred to as veins. Joints are formed by tectonic, brittle deformation as well as uplift and exhumation. Although the observed joints are not filled with mineral precipitates, most of them are mineral stained by iron oxides, occasional manganese oxides, and rare molybdenite "paint." Mineral staining typically is restricted to joint surfaces, except in areas of hydrothermal scars (Meyer and Foland, 1991; Ludington and others, 2004) and very likely attests to recent, fracture-dominated ground-water flow in the bedrock.

Figure 3 shows contoured joint orientation data plotted on equal-area projections for each outcrop studied. The shaded regions are contoured poles to joints where the darker colors represent higher concentrations of joints in a particular range of orientations. Clusters of joints that share a common orientation with some dispersion about a mean orientation can be thought of as part of a "joint set." Multiple joint sets form a joint network whose relative orientations, intensities, and apertures largely control the storage, magnitude, and direction of ground-water flow in the subsurface.

Joint networks range from simple to complex orthogonal sets as in the Tertiary sediments, Amalia Narrows, Amalia Road Cut, and Cabin Springs cliffs localities (for example, see figs. 4 and 5) to complex conjugate and random geometries such as those found in the Small Scar locality (fig. 6) and Pit Ore Body locality (fig. 7), respectively. In general, at each locality studied there is some combination of two high-angle sets, one striking northeast-southwest and one striking northwest-southeast and one subhorizontal set (fig. 3). This pattern is consistent with orientations measured from previous work at Questa (for example, Carpenter, 1968; Rehrig, 1969) as well as regionally (for example, Caine and Tomusiak, 2003).

All lithologies observed in the study area are pervasively jointed by high-intensity joint networks. Measures of joint intensity, or number of joints along a line or within an area, reported here are simple joint counts along scanlines that are perpendicular to joint-set average orientations. This type of measure tends to overestimate intensity but allows for simple counting with great rapidity and is thus appropriate for reconnaissance measures such as those applied in this study. Cumulative joint intensities of joint sets range from 55 joints per meter to 0.3 joint per meter with an average of 28 joints per meter (table 1 and figs. 4 and 7 as examples of the extremes in intensity).

Joint lengths are difficult to measure, but field estimates range from a few meters up to a few tens of meters. Numerous joints with trace lengths less than 1 meter exist in all rock types; however, these may be more significant for storage rather than flow of ground water. Joint shapes are generally curviplanar to planar, and their walls typically are smooth but may be as rough as the scale of the grains that make up the rock.

Joint apertures, or the joint wall perpendicular opening width, are probably the most elusive property to measure with any degree of meaning because joint widths vary greatly from what is observed in the surface and subsurface (for example, Snow, 1970). Yet aperture is also one of the most critical properties when linking joint-related geometric properties to their hydraulic properties (see Caine and Tomusiak, 2003, for a discussion). For the reconnaissance style of the work reported here, joint apertures were recorded merely as greater than or less than 1 millimeter. Nearly all observations indicated that open joints had apertures less than 1 millimeter, and it was exceptional to have apertures greater than a few centimeters.

Truncation refers to the way in which individual joints join or cross other joints. In general, most joints observed in all Questa lithologies were mutually crosscutting, with the exception that some of the subhorizontal sets truncated (or ended) against one of the subvertical sets, indicating that the subhorizontal sets are younger (Segall and Pollard, 1983).

Faults, Fault Zones, and Fault-Related Fracture Networks

Faults and fault zones in the Questa caldera display distinctive architectural components, or internal structures (fig. 8), that also are found in noncaldera settings. Fault-zone architectural components include a fault core, defined as the part of a fault zone where most of the strain is accommodated and that often is composed of fault rocks such as clay-rich gouge or mineralized breccias or other cataclastic rocks (Caine and others, 1996). The second common component is a damage zone that often envelops the fault core and is related to the growth of the fault zone. Damage zones are commonly

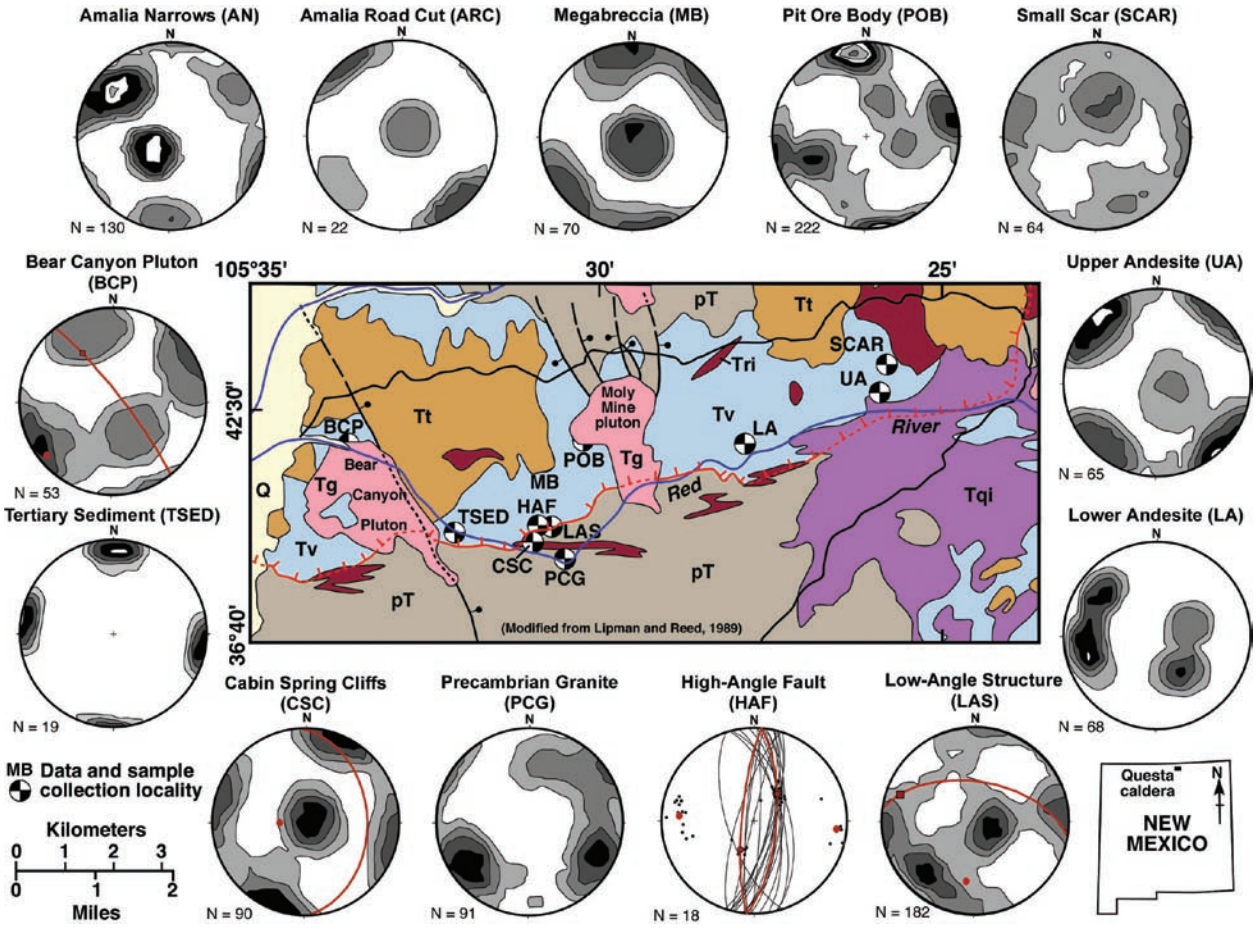

Figure 3. Southwest section of the simplified geologic map of the Questa caldera shown in figure 2 (modified from Lipman and Reed, 1989). Fracture network and fault zone data-collection localities are shown. Zones of hydrothermal alteration shown in figure 2 have been removed for clarity. Poles to fractures are shown and contoured on equal-area projections using the method of Kamb (1959). All contour intervals are 2 sigma, and N = the number of fractures measured. Mean great circles for fault plane orientations and their mean poles are shown in red. All plots were generated with the computer program "Stereonet" by Allmendinger (1995).

Table 1. Joint intensity data.

[T, Tertiary; na, not available; max, maximum; min, minimum]

Lithology	Average number open joints by set per meter	Max number open joints by set per meter	Min number open joints by set per meter	All sets cumulative average open joints per meter
T scar	na	na	na	13.5
T granite, submacroscopic	na	55	na	na
T granite, macroscopic	1.0	1.8	0.6	1.8
T rhyolite, cliffs	2.7	3.8	0.3	10.9
T rhyolite, pit ore body	5.2	6.6	1.7	20.9
T sediment	8.0	11.0	5.0	16.0
T Amalia	29.0	48.3	4.5	116.0
T megabreccia	15.8	18.0	13.3	47.3
T andesite, valley	7.1	8.7	4.0	21.2
T andesite, ridge	6.9	8.3	5.3	20.8
PC granite	3.9	12.0	2.0	11.6
All localities	**8.9**	**55**	**0.3**	**28.0**

Figure 4. View looking south at open joints with simple orthogonal orientations at the Tsed locality a few meters above the main Red River channel. Poorly developed subhorizontal joints and vertical near perpendicular joints are also present in the outcrop. Note the accentuation of apertures in the vertical joints, probably due to weathering at the surface. The outcrop is approximately 3 meters wide.

Figure 5. Oblique view of complex orthogonal open joints at the Amalia Narrows locality at the edge of the main stream channel. Note the white precipitate along the margins of joints that may have formed due to surface tension as the stream receded after a recent storm or due to seepage from the joints themselves.

Figure 6. View looking down on joints with conjugate geometry at the Small Scar locality. Although extensively hydrothermally altered, the joints are open. Conjugate geometry of the joints suggests they are tectonic in origin.

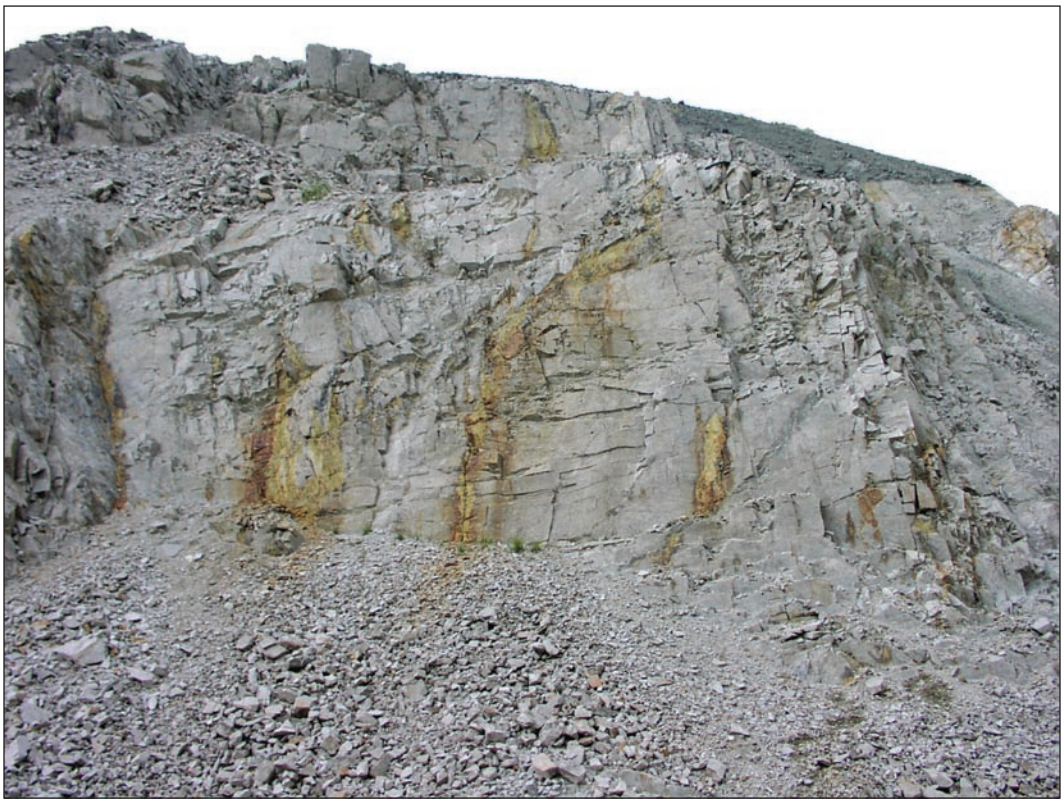

Figure 7. Example of a high-intensity, highly interconnected joint network found in the Pit Ore Body locality. Note the discrete iron oxide stains. Although this is a highly interconnected network, the stains may be indicative of the highly discrete nature of the few hydraulically conductive fractures likely to be found in the subsurface groundwater flow system.

Table 2. Fault-related damage zone fracture intensity data.

[T, Tertiary; rhy, rhyolite; sed, sediment; na, not available; max, maximum; min, minimum; DZ, damage zone; HW, hanging wall; Avg., Average]

Fault zone, location, lithology	Avg. number open fractures by set per meter	Max number open fractures by set per meter	Min number open fractures by set per meter	All sets cumulative average open fractures per meter
Low-angle fault, upper plate DZ, Tsed	15.3	16.7	14.0	30.7
Low-angle fault, upper plate DZ, Trhy	16.3	23.0	9.5	32.5
Low-angle fault intersection with high-angle fault, upper plate and HW DZ, Tsed	10.5	13.0	8.0	21.0
Low-angle fault, lower plate DZ, PC granite	3.5	4.2	2.8	10.5
Small fault DZ, Tsed, Upper Cliffs	37.0	na	na	na
High-angle fault DZ, Trhy, pit ore body	70.0	na	na	na
High-angle-long trace length, small faults, Trhy, Cabin Springs cliffs	55.0	na	na	na

composed of open and mineralized fractures, small faults, folds and other strain features (Caine and others, 1996; Knipe and others, 1998). The core and damage zone are further enveloped by the relatively undamaged host rock or protolith. Fault-zone components not only are distinctive structural heterogeneities but also can be distinctive hydrogeological heterogeneities that may impart significant anisotropy within a ground-water flow system (Sibson, 1994; Caine and Forster, 1999). Characterization of fault-zone architectural styles can be used to infer potential hydraulic behavior of faults where real hydraulic data (for example, from wells) are not available. The following field-based descriptions of the prominent types of fault zones in the study area are used later in this report to make simple Darcy calculations as estimates of fault-zone hydraulic behavior.

Fault-zone architectural styles, or combinations of each of the components, result in distinctive types of fault zones. Composite deformation zones (CDZ) have both common fault-zone components: a core and a damage zone surrounded by the protolith. Example fault-related permeability structures might include the composite deformation zone where the core is low-permeability gouge and higher permeability open fractures in the damage zone, making the fault zone a combined conduit-barrier to ground-water flow where flow is enhanced parallel to the strike of the fault but impeded across the fault. Conversely, a distributed deformation zone (DDZ) may act as a conduit relative to the protolith if many of the internal fractures are open.

Characterization of fracture networks from surface exposures may not completely represent what is in the subsurface due to the near-surface formation of exhumation-related fractures. However, tectonic fractures, faults, fault zones, and fault-related fractures are likely to be well represented in outcrop exposures as these structures originally formed at depth unlike exhumation-related fractures. The aperture of fault and nonfault-related fractures, a major control on permeability, may change with depth and is dependent on the orientations of the fractures with respect to the magnitude of overburden load as well as the magnitude and orientation of in-situ tectonic stresses at progressively greater depths (Davis and Turk, 1964; Barton and others, 1995). Depending on orientation relative to the stress field, some fractures may close down while others may become wider. Although no attempt has been made to account for stress-related changes in fracture aperture, the range of model results presented here using Darcy calculations likely covers the range of effects due to stress-related aperture changes from the surface to the depths encountered in the underground mine workings.

The spacing or intensity of faults and fault zones, as well as their associated fracture networks, also is expected to be well represented in outcrop exposures and from geological mapping. Again, this is due to their tectonic origin that is largely unaffected by near-surface exhumation-related processes. Fault and fault-zone trace-length displacement relationships as well as theoretical fracture mechanics dictate that the approximate three-dimensional shapes of faults in the subsurface can be generally understood from characterization of trace length (Cowie and Scholz, 1992). Fault tip lines, the edge of a fault or fault zone where displacement goes to zero, are likely similar to rough-edged ellipses to rough-edged rectangles (Shipton and Cowie, 2001). Given the reasonable assumption that our fundamental understandings of the tectonic history and processes that form faults, fault zones, and fault-related fracture networks apply to these structures

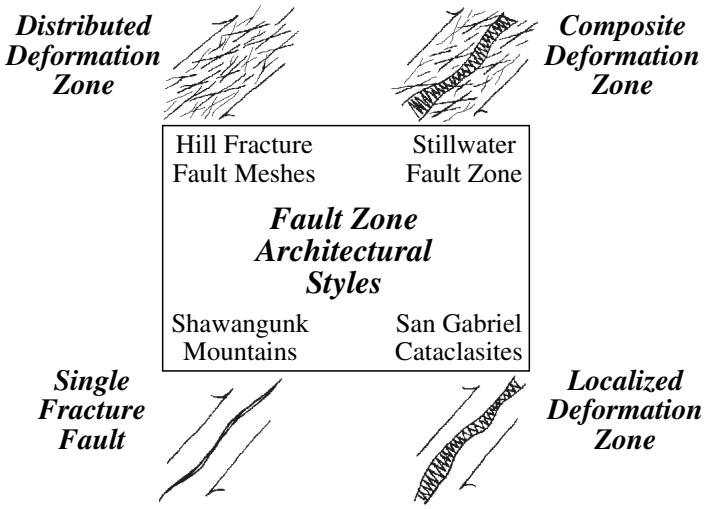

Figure 8. Conceptual diagram of distinctive fault-zone architectural styles found in nature (from Caine and Forster, 1999).

in the subsurface, most of the faults observed in the Questa caldera at the surface—high intensity in their presence with extensive 10s to 100s of meters trace lengths and meters to 100s of meters of displacement—extend well into the bedrock and are likely also present at depth with geometric, structural, and hydrological characteristics similar to what is observed in outcrop.

On the basis of field observations it appears that the major fault zones in the Questa caldera are either composite deformation zones or relatively narrow, distributed deformation zones. Host-rock lithology at Questa clearly has a large influence on fault-zone architectural style, as does the type of fault. Two end-member types of fault zones are found in the study area, consistent with mapping and observations made by Lipman and Reed (1989), Meyer and Foland (1991), and Meyer and Leonardson (1997). These include low-angle and high-angle faults, some of which form the primary structural and lithologic margin of the southern Questa caldera (figs. 2, 3, and 9).

Low-Angle Structures

One outcrop of an exceptionally well exposed, east-west-striking, low-angle structure was found (J.W. Meyer, Hanover College, Santa Maria, California, oral commun., 2001). Other low-angle features were found in several localities (figs. 3 and 9); however, only a few were faults, and most were either subhorizontal joints, volcanic unit flow boundaries, possible hydrothermal fluid conduits, or colluvial deposit contacts with bedrock. This observation is significant because there probably are only several low-angle, major fault zones in the study area, and thus they may be only highly localized hydrogeological heterogeneities most commonly associated with the caldera margin.

The well-exposed low-angle fault zone also is mapped as the caldera structural margin (Lipman and Reed, 1989; Meyer and Leonardson, 1997). Although the geological significance and history of this structure are important, further assessment is not within the context and focus of this report. Interested readers are referred to Meyer and Leonardson (1997) for a discussion on this topic. This structure shows an upper-plate damage zone composed of highly fractured, near-vertical septa of Tertiary rhyolite within the Tertiary pebble-to-boulder conglomerate (see figs. 3, 9, and 10 and compare Trhy and Tsed fracture intensities from tables 1 and 2). Fracture intensity in the rhyolite is uniformly higher than in the sediment where high-intensity fracturing is more localized. Fracturing in the upper-plate damage zone shows a strong clustering of high-angle, northwest-southeast- and north-south-striking open fractures. In stark contrast, the lower-plate damage zone, composed of Precambrian granite, shows fracture intensities no greater than its relatively undeformed protolith (tables 1 and 2).

As the fault core is approached from the damage zone, the deformation and hydrothermal alteration appear to increase in both the rhyolites and sediments in the upper plate and similarly in the Precambrian granite in the lower plate (figs. 10, 11, and 12). The damage-zone upper and lower contact is in sharp contact with the fault core and is demarcated by polished and striated, silicified slip surfaces with kinematic indicators dominantly indicating upper-plate, west to east motion; however, several steps on slip surfaces also indicated upper-plate east to west motion (figs. 3 and 13). This may indicate reactivated, incremental strain events and(or) possibly accommodation of local strain from emplacement of the Tertiary rhyolite dikes in the upper plate (fig. 10).

The central fault core itself is composed of foliated pods of highly sheared and mixed clay-rich gouge and cobble-conglomerate fault gouge in which some Tsed quartz-rich cobbles are essentially survivor clasts that are highly fractured

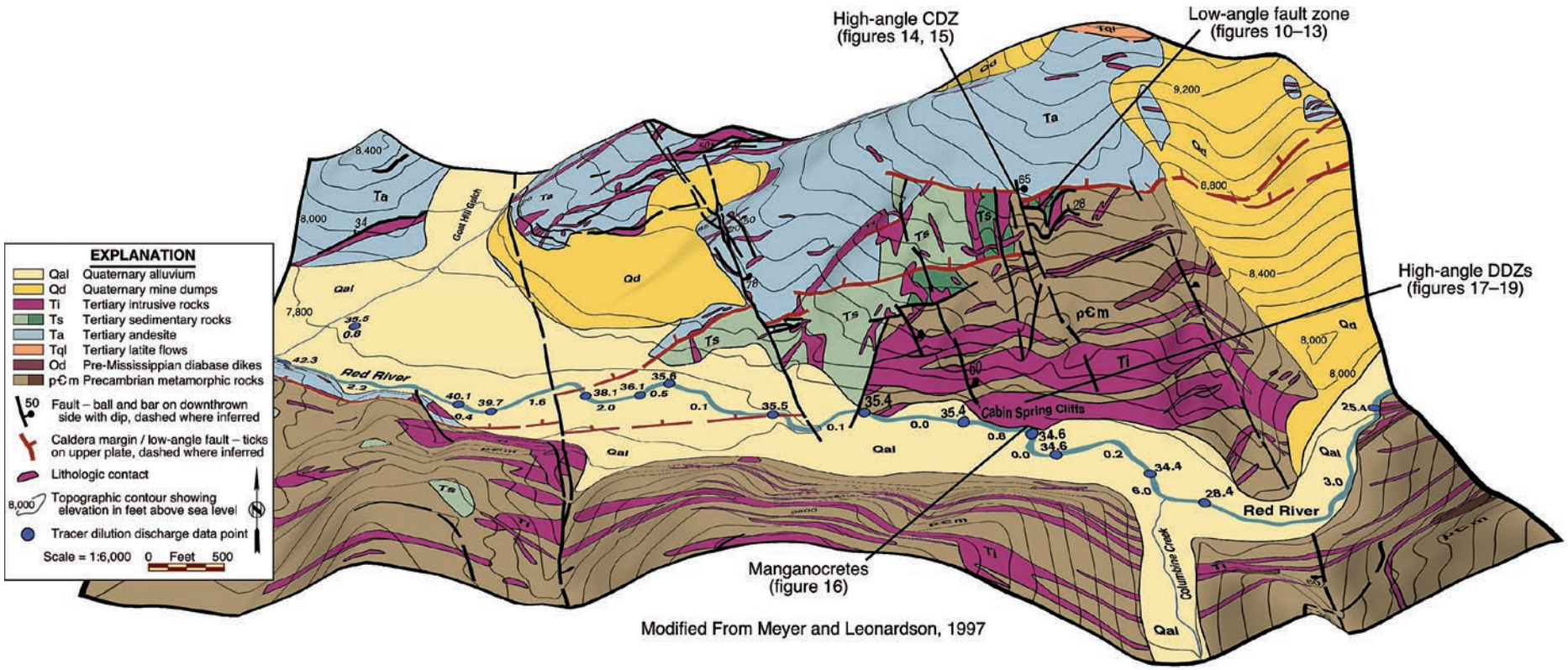

Figure 9. Geologic map modified from Meyer and Leonardson (1997) and draped onto a 30-meter digital elevation model with no vertical exaggeration and a 100-foot contour interval. Geologic units, geologic structures, their possible geomorphic expressions, and the Red River in the vicinity of Cabin Springs cliffs, Columbine Park, and the Goat Hill fan are shown. The locations of some outcrops studied in detail and for which there are photographs in the text are shown. These include the exceptionally well exposed low-angle structure and its intersection with the high-angle fault that cuts it and drops the caldera margin (red hachured line) down to the east, the Cabin Springs cliffs small fault network, and manganocretes on the north bank of the river. Discharge (Q) data from the USGS 2001 base-flow tracer dilution study (McCleskey and others, 2003) are shown as blue dots along the river. Values in cubic feet per second at the blue dots are the calculated Q value for that point. The Q values between the dots are the difference between the upstream and downstream values.

(figs. 11 and 12). The phacoidal (lens-shaped in three dimensions) cleavage is highly foliated with an anastomosing fabric subparallel to the dominant orientation of the major fault zone. This cleavage conforms into the bounding slip surfaces, leaving little open space. The magnitude of displacement on this fault is undetermined due to a lack of piercing points. The various gouges in the fault also appear to have been chemically altered, and no field-scale manganese oxides were found in this structure.

The extensive, high-intensity, open-fracture networks in the upper-plate damage zone relative to the host rocks and the clay-rich fault core bounded by silicified slip surfaces suggest that this fault probably acts as a combined conduit-barrier to ground-water flow (fig. 8). Because of the few good exposures of the caldera margin in the study area, it is hard to determine how similar or different the structural architecture of other parts of the caldera margin may be, or if this type of structure is representative of other caldera structural margins in general.

High-Angle Composite Deformation Zones

Directly adjacent to the low-angle structure is a high-angle, north-south-striking extensional fault that cuts and displaces the low-angle structure (figs. 3, 9, 13, and 14). The footwall of the high-angle fault is Precambrian granite, and the hanging wall is the upper plate of the low-angle structure. Below the upper plate/lower plate contact of the low-angle structure the rocks are largely buried, making it difficult to determine their interrelationship. However, a minimum dip-slip displacement (see figs. 3, 9, and 14) of 14 meters, top down to the east, was measured between exposed Precambrian piercing points.

The footwall and hanging-wall damage zones in the adjacent high-angle fault zone are composed of open fractures and some quartz veins; however, the fracture intensities were not exceptionally higher than the background jointing in the granites. The damage-zone fracture orientations are mechanically compatible with an Andersonian-style high-angle extensional fault (fig. 3 and Caine and Forster, 1999). The fault core is composed of matrix-supported fault breccia and quartz-rich gouge with granite clasts surrounded by highly polished, striated, silicified, and corrugated slip surfaces into which the breccia and gouge are highly conformed, leaving little visible open space (fig. 15). An inner core also shows stringers and veins, subparallel to the fault core, that are composed of highly weathered iron and manganese oxides. These fault-core materials have undergone brecciation, suggesting that the oxides were originally emplaced prior to faulting and possibly are synmineralization.

Local vuggy zones along the eastern fault-core damage-zone contact have clusters of centimeter-scale, calcite crystalline masses thickly coated with iron and manganese oxides. Few oxide mineral veins or stringers associated with faults were found anywhere in the vicinity of the core of this composite deformation zone. The only other place manganese oxide was found was as sparse coatings in small faults in rhyolite, discussed herein.

The architectural style of this fault can be classified as a composite deformation zone, as in Caine and Forster (1999). This architectural style may indicate that the fault zone is a present-day combined conduit-barrier, with ground-water flow enhanced parallel to the fault but impeded across it. Although

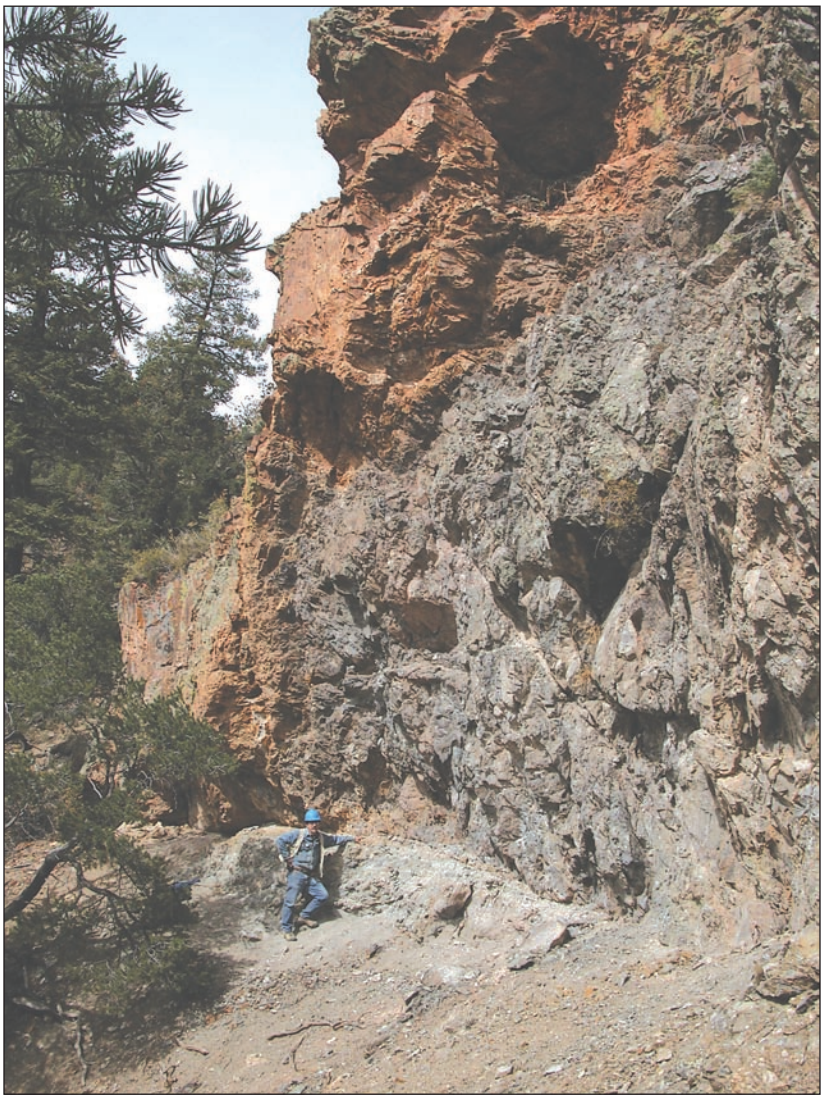

Figure 10. Low-angle fault zone (the core is at the person's shoulder) looking approximately west, showing Tertiary rhyolite (red) and boulder conglomerate (gray-brown) in the upper plate and Precambrian granite in the lower plate. The high-angle extensional fault discussed in the text is exposed in the far left side of the photograph. See figure 9 for map location.

Figure 11. Fault damage zone of the low-angle fault zone at the location of the person's shoulder in figure 10. The lower plate is composed of hydrothermally altered Precambrian granite, and the upper plate in this photograph is composed of hydrothermally altered Tertiary boulder conglomerate. Note the multicolored, clay-rich fault gouge that separates the upper and lower plates.

Figure 12. Closeup view of phacoidally cleaved, white, red, and black, clay-rich fault gouge in the low-angle fault-zone core. Note that the two-dimensional long axis of the phacoidally cleaved gouge is parallel to the major orientation of the curviplanar primary slip surfaces and that this central-core zone has a very sharp upper and lower contact with the upper- and lower-plate fault rocks and damage zones.

Figure 13. Closeup view of silicified, polished, and striated slip surfaces that mark the contact of the upper and lower plates of the low-angle fault zone. This slip surface is part of a complex network of slip surfaces that are both subhorizontal and subvertical but indicate west-east motion.

Figure 14. View looking south of the high-angle fault zone that intersects the low-angle fault zone at the lower left-hand corner of this photograph. Note the highly polished and striated white slip surfaces that form the footwall contact of the fault core and Precambrian granite footwall damage zone. See figure 9 for map location.

the fault-core silicified breccias are cemented, the presence of localized vuggy zones and oxidized veins or stringers indicates that there may have been, and still may be, highly localized ground-water flow within and parallel to the fault core. The observation that the fault-core oxide mineral veins are brecciated and thus possibly are synmineralization in origin strongly suggests there has been a persistent and localized source of iron and manganese present at this location prior to and during the postglacial formation of the Red River Valley. This is consistent with the presence of manganocretes, or manganese-oxide-cemented alluvial deposits, along the banks of the Red River, particularly at Cabin Springs directly below this fault (fig. 16).

High-Angle Distributed Deformation Zones

In contrast to the high-angle faults in the Precambrian granites and the low-angle fault system, there are numerous high-angle, north-south- to northwest-southeast-striking, extensional, small displacement faults in major rhyolite dikes and the Tertiary Bear Canyon granite pluton (figs. 3, 9, 13, 17, and 18).

Many of these high-angle, small fault zones also cut the Precambrian granite, but there were few outcrops where the styles of these faults could be directly characterized in Precambrian host rocks. The predominant difference in the Tertiary rhyolite small faults compared to the high-angle composite deformation zones in Precambrian granites and the low-angle caldera margin structure, discussed previously, is that the faults in rhyolite are dominantly open, unmineralized structures. The rhyolite small faults range in style from curviplanar single-fracture faults with no damage zones to bounded zones of open fractures up to 1 meter wide (figs. 8 and 19). The cores of these faults are bounded by moderately polished and striated slip surfaces, and where dilated, the core is composed of extensive, distributed brittle fracturing of host rock with conjugate geometry; there is no fault gouge or breccia (fig. 19). Several of the high-angle rhyolite faults exhibit sparse and spotty, black mineral surface coatings that are dendritic and indicative of the drainage of manganese oxide-rich water through these faults. This staining is not part of or within the fault rocks as they are in the high-angle composite deformation zone described previously.

Displacement along these faults, both synthetic and antithetic in comparison with the high-angle composite deformation zone discussed herein, is less than about 2 meters. Particularly extensive, dominantly high-angle, north-south- to northwest-southeast-striking, distributed deformation in the form of open fault-related fractures was observed in the tip zones of this style of fault. In one particularly well-exposed cliff face (the Cabin Springs cliffs, figs. 9 and 17), fault intensity was measurable along a linear traverse, indicating that there was approximately one high-angle, small displacement fault every 10 meters on average (table 3; note that in fig. 9 not all of the small faults observable in the cliff were mapped by Meyer and Leonardson, 1997). The architectural styles of these small faults characterize them as distributed deformation zones (fig. 8) and suggest they act as important conduits for ground-water flow parallel to their strikes.

An exception to the open nature of the fault cores in the rhyolites is the small faults in the ore body itself. Figure 20 shows a well-developed small fault in the rhyolite ore body found in the Molycorp pit. The fault core is composed of a molybdenite-infilled cataclasite, and the slip surface is striated "moly paint" as commonly observed by Carpenter (1968), Clark (1968), and Rehrig (1969). However, several of these faults do show narrow, iron-oxide-stained damage zones with some open fault-related fractures as shown in figure 20, making them composite deformation zones whose architecture is likely to be related to their proximity to the main ore body.

Table 3. Small fault intensity data.

[T, Tertiary; rhy, rhyolite; sed, sediment]

Location, fault type, lithology	Total number open faults observed	Traverse length (meters)	Average number open faults per 10 meters
Cabin Springs cliffs, high-angle, long trace length, small displacement faults, Trhy and Tsed	11	66.9	1.6
Upper cliffs, high-angle, long trace length, small displacement faults, Trhy and Tsed	9	43.8	2.1

Figure 15. View looking north at the fault core of the high-angle fault zone. Note the silicified breccia in the core.

Figure 16. Manganocrete deposit (iron and manganese oxide-cemented alluvial and colluvial materials) at the base of the Cabin Springs cliffs on the north bank of the Red River. See figure 9 for map location. Photograph courtesy of Phil Verplanck.

Figure 17. View looking north at the Cabin Springs cliff rhyolite dike that strikes parallel to the plane of the photograph and is cut by open and relatively small extensional faults that strike perpendicular to the plane of the photograph. Note the subhorizontal basalt dike, shown by the red arrow, that cuts the rhyolite and is cut by the high-angle faults showing offsets on the order of a meter. See figure 9 for map location.

Figure 18. View looking north at small faults, fault-related fracture networks, and near-orthogonal joint sets in the Bear Canyon pluton at the mountain front and the west end of the Red River Valley.

Figure 19. View looking north at the fault core of a small fault in the Cabin Springs cliffs. Displacement is less than 1 meter, and the fault core is composed of open and extensive, conjugate-style, fractured rhyolite host rock.

Figure 20. Small extensional fault and primary slip surface in the lower pit ore body showing "moly paint" and iron oxide staining that is probably related to recent seepage and open fractures in the footwall damage zone.

Other Potential Structural and Hydrogeologic Heterogeneities in the Questa Caldera

The Caldera Margin and Ground-Water Flow

Although exposures of the structural margin of the Questa caldera are minimal in the central and western Red River Valley, observations from mapping and the exceptional low-angle fault-zone exposure discussed previously show that this margin is a major lithologic and structural heterogeneity (Lipman and Reed, 1989; Meyer and Leonardson, 1997; figs. 9 and 21). Due to a lack of exposure, of drilling records from boreholes, or of data from mine workings that may have penetrated this margin, its true architectural form and the consistency of that form are unknown. However, one might speculate that, because of the displacement accommodated along this margin, its coincidence with intrusive and extrusive igneous activity, and its major lithologic juxtaposition, the margin is a highly complex hydrogeological feature that probably varies spatially between any one of the major end-member permeability structures—barrier, conduit, or combined conduit-barrier (fig. 8).

The Red River Valley east-to-west downstream topographic gradient is steep (average about 0.02) and the north-south valley walls are steeper yet (north side average about 0.2, figs. 9 and 22). Because these topographic gradients translate into potential hydraulic head gradients that drive ground-water flow, ground-water flow lines should converge along the thalweg of the Red River (for example, Hubbert, 1940, and fig. 22) and in three dimensions should have components of downvalley, lateral flow as well as upward flow from the bedrock to the stream.

The caldera margin crosses the Red River in three places as mapped (figs. 2 and 9), and given the previous observations regarding the brittle deformation associated with the margin where it is exposed, one might surmise that it could act as a zone of enhanced bedrock ground-water flow. However, the actual extent of bedrock ground-water discharge to the Red River is dependent not only on the gradients but on the bulk permeability structure of the bedrock itself relative to the bulk permeability of features such as the margin structure, faults that might cut it, and the overlying surficial deposits within the thalweg of the river.

Stockwork and Other Vein Systems

Several other geologic structures were observed that may be significant with respect to the Questa ground-water flow system. These include stockwork-style quartz and pyrite veins in Tertiary andesite as well as planar to curviplanar, manganese oxide-stained, north-south-striking quartz vein swarms in the Precambrian granite. The stockwork veins were pervasive in localized sections of andesite found in the thalweg of Straight, Hottentot, and two unnamed creeks. The quartz vein swarms were found in only two out of about eight outcrops of Precambrian granite, indicating they are localized. Numerous opening-mode and fault-related molybdenite veins and faults were also observed in ore-body-related Tertiary rhyolite in the Molycorp pit, as noted herein. The closed veins showed the full gamut of orientations but showed a dominance of northeast-southwest and northwest-southeast strikes and high to moderate dip angles, as noted in detail by Rehrig (1969).

Lithologic Contacts

Although few lithologic unit contacts were observed, these features may be hydrogeological heterogeneities due to open discontinuities between them. In the caldera system there are likely to be complex unit contacts that may fall into two

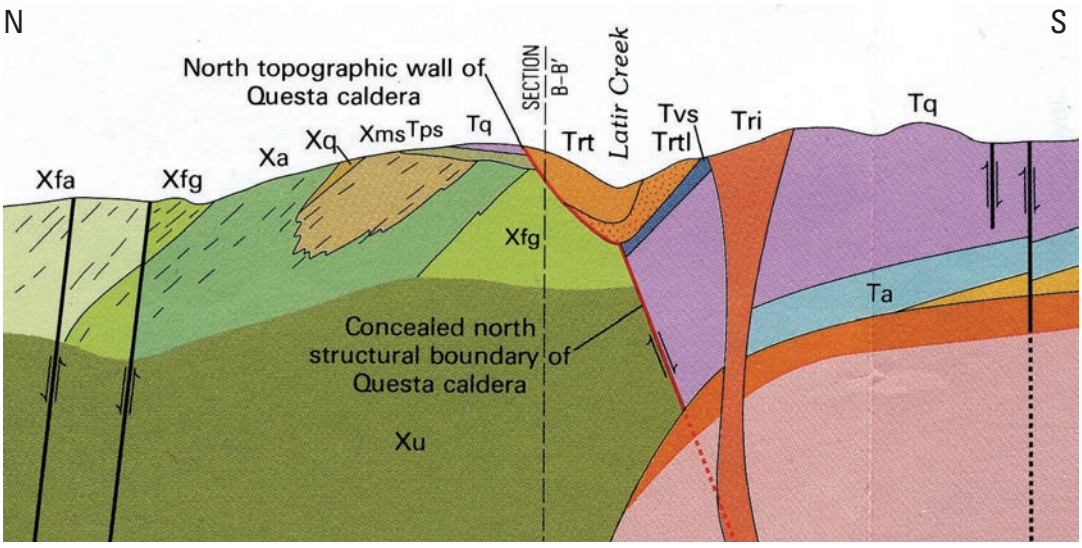

Figure 21. Segment of a geologic cross section from the geologic map of the Latir volcanic field including the Questa caldera from Lipman and Reed (1989). Although this section is from the northern part of the caldera, the margin is clearly noted as a major lithological heterogeneity and extensional fault, and it is likely to be similar to that found in the Red River drainage.

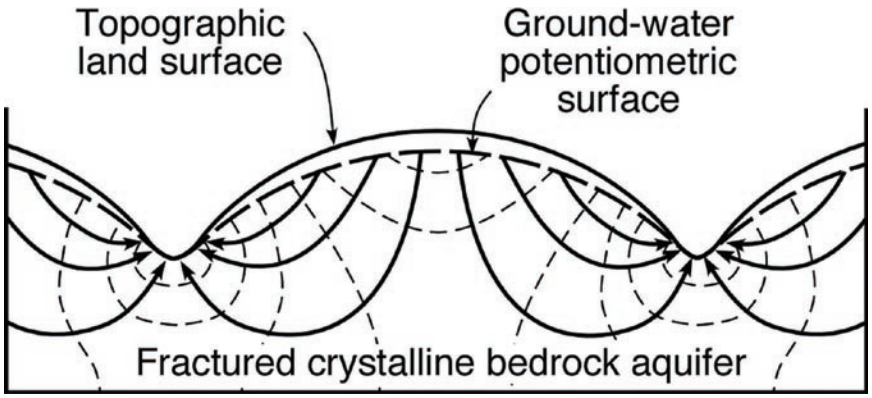

Figure 22. Two-dimensional, cross-sectional ground-water flow net for a region with high gradients and an isotropic, homogeneous bedrock aquifer at the bottom of which there is a no-flow boundary (after Hubbert, 1940). Hydraulic theory dictates that in three dimensions there will be flow lines coming out of the page due to an up-gradient hydraulic head associated with higher and lower regions along the valley thalweg.

end-member styles: intrusive and extrusive or flow contacts. Observed intrusive contacts showed no open space and thorough welding. Joint networks that cut these contacts generally were not perturbed by the contact itself, and thus this type of contact may be transparent hydrologically (see Caine and Tomusiak, 2003). In contrast, extrusive contacts such as those found between various types of pyroclastic, andesite, or debris flows deposited on previously cooled units may be sufficiently rough as to provide open space for ground-water flow and thus may be localized conduits.

The Range-Front Fault Zone

At the mountain front to the west of the Molycorp mining operation, the Red River crosses a poorly exposed range-bounding extensional fault zone (Lipman and Reed, 1989, and fig. 3). Although the poor exposure does not allow for direct observation of the core or cores of this fault zone, one can observe what probably is part of the footwall damage zone in the westernmost exposures of the Bear Canyon pluton (figs. 3 and 18). As previously discussed, numerous small faults as well as pervasive, high-intensity joint networks are present.

Faults in Surficial Deposits

Although beyond the scope of this study, faulting in the alluvial and colluvial materials and their potential interactions with bedrock fault zones may be an important part of the hydrogeological story in the Red River Valley, particularly at the range front. If presently active surface-rupturing faults along the range-front fault system cut recent sediments of the Santa Fe Group and(or) younger surficial deposits, these active faults also may be involved with controlling mountain block, mountain front, and in-stream recharge processes in the Rio Grande basin. Presently active faults in the basin-fill sediments may be important heterogeneities in the context of solute transport of acidic and metal-rich water to the basin aquifer system. No attempt, however, has been made in this study to characterize such fault zones.

Insights from Estimation of Bedrock, Caldera Margin, and High-Angle Fault-Zone Permeability Structure

Introduction to Computations

Common conceptual models for fractured, crystalline bedrock aquifer systems include the idea that there is a highly fractured and weathered upper, high-conductivity zone that grades into lower and lower conductivity rocks with depth (Davis and Turk, 1964; Snow, 1972; URS, written commun., 2001; Caine and Tomusiak, 2003). Although this type of bedrock aquifer system commonly has low bulk hydraulic conductivity, it can be heterogeneous and have zones of considerable conductivity, as shown in table 4, from aquifer hydraulic tests in the area of the mine as well as being consistent with values cited for other fractured bedrock aquifer systems (for example, approximately 10^{-4} to 10^{-8} m/s as reported in Freeze and Cherry, 1979). Characterization of the permeability structure of a complex bedrock aquifer system, such as that found in the Red River watershed, should ideally be based on (1) hydraulic data from wells derived from pumping tests within those wells, (2) time series water-level data from wells, (3) carefully designed measurements of natural and perturbed ground-water flow from mine tunnels initiated at the time the mine was originally constructed to monitoring through the life of the mine, (4) ground-water flow and discharge data from stream base flow and spring measurements, (5) surface meteorological data such as precipitation and evapotranspiration data, (6) geochemical data that can help constrain unique water/rock interactions between geological units or features, (7) geological data that identify potentially significant geological features that might cause heterogeneity within the aquifer system at various scales or that tie hydraulic data to geological reality, and (8) numerical ground-water flow modeling at appropriate scales with appropriate levels of detail that are used to progressively integrate the various types of data cited herein and to investigate the effects of simple and complex model realizations in order to better understand the system as a whole. Unfortunately, at Questa, many of the cited data are not available, and thus the use of simple Darcy calculations is warranted as a means of obtaining a first-order

Table 4. Reported bedrock hydraulic data for the region around the Questa mine and the USGS Straight Creek research site.

[* See References Cited for footnoted sources. ** Test types: S, slug; P, single well pumping; R, single well recovery. K, hydraulic conductivity]

	Well ID	Source*	Type of test**	Lithology	K (m/s)	Total depth (m), depth to bedrock (m), screened interval (m), and notes
Region Near the Mine	MMW-3	1, 3, 7 1, 3, 7	P R	Andesite	1.4E-07 2.5E-08	44.2 17.7 19.8 to 35.1
	MMW-7	1, 2, 7 1, 3, 7 1, 3, 7	S P R	Andesite	9.4E-08 3.1E-08 4.7E-09	49.1 25.6 26.2 to 49.1
	MMW-11	1, 3, 7 1, 3, 7 1, 3, 7	P P P	Monzonite	1.1E-03 2.4E-06 3.0E-04	44.2 56.4 44.1 to 56.4
	MMW-17B	2, 5, 7	S	Andesite and rhyolite	2.1E-05	42 26.8 37.2 to 41.8
	MMW-18B	2, 5, 7	S	Granite	7.5E-06	37.5 25.3 27.1 to 36.3
	MMW-19B	2, 5, 7 2, 5, 7 2, 5, 7	S P R	Andesite	5.4E-06 2.5E-07 1.8E-07	59.6 47.5 49.8 to 59.0
	MMW-23B	2, 5, 7 3, 5, 7 3, 5, 7	S P R	Welded tuff	1.1E-06 3.6E-08 3.6E-08	30.1 3.7 20.4 to 29.6
			K Statistics	maximum minimum geo mean	2.1E-05 4.7E-09 2.2E-07	Statistics do not include MMW-11 due to lack of drawdown during the aquifer test
USGS Straight Creek Research Site	SC-1B	7 7 7 7 7	S S S S S	Volcanic rock, likely andesite	3.7E-07 4.4E-07 6.3E-07 8.0E-07 1.6E-07	44.5 25.6 39.6 to 42.7
	SC-2B	7 7 7 7 7	S S S S S	Rhyolite	1.6E-07 1.1E-06 1.5E-07 9.5E-07 5.4E-08	26.2 16.8 (WB) and 26.2 (CB) 18.4 to 26.1 Screened in weathered (WB) and competent (CB) bedrock
	SC-3B	7 7 7 7 7 7 7 7 7	S S S S S S S S S	Volcanic rock, likely andesite	6.7E-08 8.3E-08 1.1E-07 1.6E-08 2.0E-08 2.7E-08 3.3E-08 1.3E-06	60.96 32.6 49.1 to 58.2
	SC-5B	7 7 7 7 7 7 7	S S S S S S S	Latite	1.8E-06 2.2E-06 2.9E-06 1.2E-06 1.6E-06 1.9E-06 2.5E-06	128.0 86.9 103.0 to106.1
			K Statistics	maximum minimum geo mean	2.9E-06 1.6E-08 3.2E-07	

understanding of the complex ground-water flow system and its various heterogeneities.

Numerous geological features exist that may cause hydraulic heterogeneity in the Questa bedrock aquifer system (figs. 9 to 20). Several reports indicate variations in hydraulic properties of the bedrock aquifer system, as well as evidence for bedrock-derived ground-water discharge into the Red River and Red River alluvial aquifer in the vicinity of the Cabin Springs cliffs (for example, South Pass Resources, Inc., written commun., 1995; GSi, 1996; Slifer, 1996; Abshire, 1998; Vail Engineering, Inc., 2000; URS, written commun., 2001; and McCleskey and others, 2003; Kirk Vincent, written commun., 2005; also see fig. 9). However, few hydraulic data exist that robustly link bedrock hydraulic properties to specific bedrock structures, other heterogeneities, and the extent and spatial scales to which these heterogeneities behave as discrete and(or) continuum-type controls on ground-water flow at various spatial scales except in a fashion that is highly generalized. To understand the significant, relative contributions of bedrock ground-water flow to the alluvial aquifer and the Red River, the potential heterogeneities can be grouped into a hierarchical order of possibilities. The dominant and most probable geological features that may contribute to ground-water discharge include (1) the bedrock itself, inclusive of the various joint networks previously described (discussed in South Pass Resources, Inc., written commun., 1995a); (2) the caldera-margin fault zone; and (3) the high-angle, small-displacement faults (figs. 8 to 19).

Because there is no way to directly measure the ground-water flux through a sufficiently large volume and at an appropriate scale, a simple alternative approach is to use Darcy's law to estimate hydraulic properties for the various geologic features described. Darcy's law can be utilized in its form:

$$Q = KIA \tag{1}$$

where Q is the volumetric flow rate [with fundamental dimensions L^3/T; L = length, T = time], K [L/T] is the bulk hydraulic conductivity of the geological feature of interest, I [dimensionless] is the hydraulic gradient, and A [L^2] is the specified cross-sectional area across which the discharge, Q, flows.

Calculations based on equation 1 assume primarily that the media through which flow occurs can be treated as an isotropic, homogeneous continuum where mass is conserved and where there are no driving forces other than gravity. Potential fracture aperture closure due to overburden load or tectonic stress is not accounted for, but the results are likely reasonable for the relatively near surface environment between the surface and underground workings of the mine in the vicinity of the Cabin Springs cliffs. Additionally, these computations would primarily represent a paleo or premining, unconfined bedrock ground-water flow system where effects from the present-day open pit and pumping from the underground mine workings are not accounted for. For example, South Pass Resources, Inc. (written commun., 1995), GSi (1996), and Abshire (1998) indicate that at least some component of the present-day bedrock ground-water flow gradient in the vicinity of Cabin Springs cliffs and springs is away from the river, to the north, due to mine-related pumping.

However, a bedrock potentiometric-surface map constructed by URS (written commun., 2002) shows a ground-water capture zone related to dewatering of the underground mine workings. The mine workings are nearly a kilometer and a half away in a northwest direction from the Cabin Springs area. Directly to the north of Cabin Springs, the map shows a minimum of 240 meters of mapped potential hydraulic head above Cabin Springs. In addition, there is a large unmapped area with potential hydraulic head that is above and continues to the north of the mapped area. This area—without underground workings below it—extends an additional kilometer and a half and more than 300 vertical meters above Cabin Springs and the mapped area (URS, written commun., 2002). This represents a significant volume of likely saturated bedrock aquifer above Cabin Springs today with hydraulic gradients similar to those used in the theoretical computations. This gradient and volume of saturated aquifer could provide bedrock ground-water flow that is consistent with the model results reported by Kirk Vincent (written commun., 2005) inclusive of the underground workings and the open pit. Although the URS (2002) potentiometric map is statistically derived from only a few water-level data points between the surface projection of the underground workings and Cabin Springs, the data show a significantly large mound of ground water between the underground mine workings and the river. This mound would create a ground-water divide between the workings and the river that could cause some component of flow from the north of Cabin Springs to the river as well as away from the river. At this time, however, the actual geometry of the dewatering-related capture zone is poorly constrained in this area.

Although there is uncertainty regarding the effects of mine dewatering on the bedrock flow-system gradient, it is clear that ground-water discharge has interacted with the bedrock in the past (for example, the manganocretes in fig. 16) and likely continues to be expressed in the present as bedrock springs and seeps such as Cabin Springs. The computations also do not take into account the possibility of perched bedrock ground water that may be largely decoupled from the deeper bedrock flow system (see South Pass Resources, Inc., written commun., 1995, and Abshire, 1998). Although these computations are obvious simplifications, they do provide first-order insights into what is possible and what the contributions of the bedrock and the fault zones might be, relative to one another.

Several constraints provide a unique opportunity to use this approach for the Cabin Springs area. On the basis of U.S. Geological Survey tracer-dilution discharge data (Robert Runkel and Kirk Vincent, written and oral communs., 2005), an unaccounted-for, possibly bedrock-derived, ground-water inflow of 0.02 cubic meter per second flows into the Red River alluvial aquifer somewhere along the Cabin Springs reach of the Red River. This inflow also appears to be primarily emerging along the north side

of the river where there are no surficial-deposit aquifer units of significance (fig. 9). Vincent (written and oral communs., 2005) states that 0.02 cubic meter per second is a minimum value for the inflow. In order to cover a possible range of values in the theoretical Darcy calculations, values of volumetric flow rates (Q) of 0.01, 0.02, and 0.05 cubic meter per second were used for multiple Darcy computations. For each value of Q, estimated and varying potential hydraulic gradients (I, four arbitrary but reasonable depths to water at the topographic ridge) and cross-sectional areas (A, five cross-sectional areas constrained by the single length of the reach of the Red River along which the inflow occurs and for an estimated, yet arbitrary but reasonable, depth of ground-water circulation) for the bedrock and faults were used (see figs. 9, 22, 23, and table 5). Because there is no water table, potentiometric elevation, or cross-sectional area of ground-water circulation data available for the volume of bedrock of interest, several reasonable scenarios were chosen. Potential average topographic head gradients and suitable cross-sectional areas were measured using topographic and geologic maps and profiles (fig. 23 and table 5). This approach allows for multiple reasonable scenarios for the computation of values of hydraulic conductivity (K) to be solved for and compared to (1) reported bedrock aquifer-test values of K in the Cabin Springs area (table 4) and (2) values based on model results from Caine and Forster (1999) using the reorganized form of equation 1:

$$K = Q/IA \qquad (2)$$

The results of these computations are shown in table 5. This table shows the input values and summary statistics for all of the computations for each idealized scenario. Three plots (see figs. 25, 27, and 28) also show the reported and computed values that can be compared in order to gain insight into the potential bedrock and fault-related flow system.

Computational Results for the Bedrock

Figure 24 shows the conceptual model set up for the resulting computed values of bedrock K plotted against the depth of the cross-sectional areas (fig. 25) with a single-line length (L) that intersects the ground surface. The length of the line corresponds to the approximate reach of the Red River where the suspected 0.02 cubic meter per second of bedrock excess inflow occurs (Kirk Vincent, written commun., 2005). The actual depth of circulation is unknown; however, reasonable, albeit arbitrary, estimates from 10 to 500 meters below the ground surface are used. Using a range of Q values of 0.01, 0.02, and 0.05 cubic meter per second has the benefit of halving and slightly more than doubling the reported excess flow value. This range covers potential uncertainty in the reported flow due to geometry of the alluvial channel and temporal aspects of flow that might be caused by seasonal changes in base flow. Furthermore, using a range creates a scenario where bedrock discharges symmetrically from both the north and south sides of the Red River Valley to the Cabin Springs reach, as might be expected from a Hubbert-like model shown in figure 22. Values of K shown as blue points and associated blue lines (fig. 25) were computed for estimated minimum, intermediate, and maximum bedrock Qs, varying values of I associated with different depths to the water table at the watershed divide (figs. 24 and 25), and varying values of A, as previously discussed, using equation 2 (table 5). Reported hydraulic conductivities (K) from bedrock aquifer tests are shown as green lines of constant value.

Figure 25 shows viable solutions and intersection zones where the computational results intersect reported values of K. Intersection zones indicate a theoretically possible set of bulk K values for the model regions that could generate the reported Q values to the Red River. Figure 25 also indicates several attributes of the bedrock ground-water flow system. The vertical

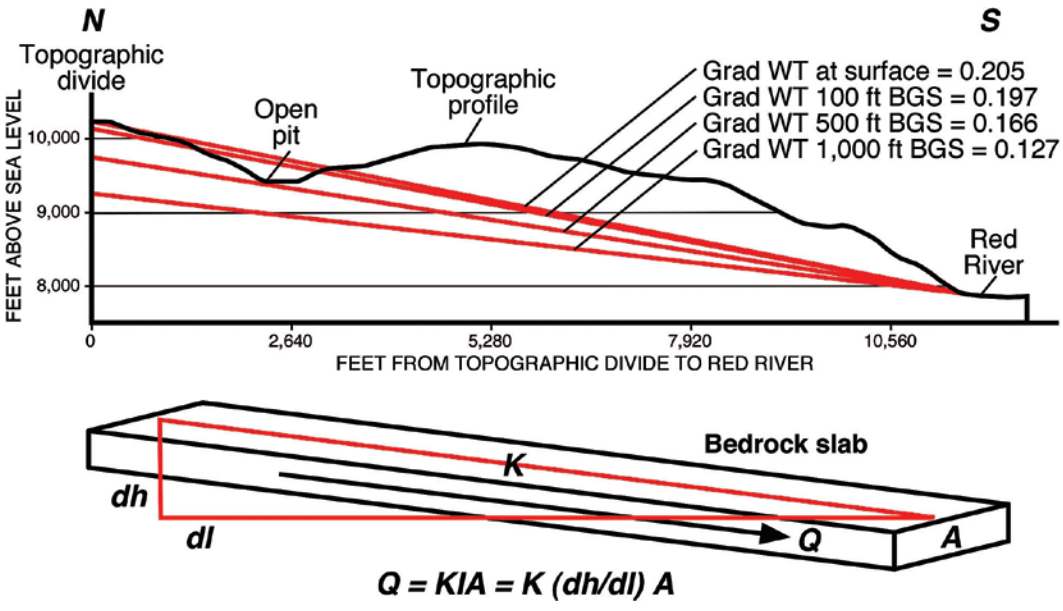

Figure 23. Schematic diagram showing an average topographic profile from the north divide of the Red River watershed to the river, average potential topographic head gradients for varying depths to water at the divide, and the geometry and parameters used for computations. Note: Grad WT refers to gradient of the water table, and BGS refers to below ground surface.

Table 5. Input data and summary statistics for computed and reported bedrock and fault zone hydraulic properties.

[*Q*, discharge; *K*, hydraulic conductivity; m, meters; s, seconds; BGS, below ground surface; geo mean, geometric mean; n, number of values; std dev, standard deviation; intersect, intersection; DDZ, distributed deformation zone; AP, aperture; μm, micrometers; RR, Red River; N, north; S, south]

Bedrock Estimates for Q Values of 0.01, 0.02, and 0.05 cubic meter per second

Note: All gradient estimates are from the northern Red River watershed divide along an approximately north-south, straight line down to the Red River (see figure 21 in text). All lengths in meters.

INPUT VALUES					SUMMARY STATISTICS		
Gradient	**Average gradient scenario**	**Surface length (m)**	**Depth (m)**	**Area (m^2)**	**Bedrock**	**Computed *K* values (m/s)**	**Reported *K* values (m/s)****
0.205	Water table at ground surface	1,210	10	12,100	maximum	3.3E-05	2.1E-05
0.197	Water table 100 feet BGS	1,210	50	60,500	minimum	8.1E-08	4.7E-09
0.166	Water table 500 feet BGS	1,210	100	121,000	geo mean	1.2E-06	2.2E-07
0.127	Water table 1,000 feet BGS	1,210	250	302,500	n	60	13
		1,210	500	605,000	std dev	6.4E-06	6.0E-06
					variance	4.1E-11	2.2E-10

Caldera and High-Angle Small Fault Estimates for Q Values of 0.01, 0.02, and 0.05 cubic meter per second

INPUT VALUES					SUMMARY STATISTICS		
Gradient	**Average gradient scenario**	**Surface intersect width (m)**	**DDZ depth (m)**	**Area (m^2)**	**Faults**	**Computed *K* values (m/s)**	**Reported model *K* values AP & geo mean (μm), (m/s)**
0.349	N low-angle fault (3) segment to RR	10	10	100	**Caldera margin fault zones**		
0.201	N low-angle fault (2) segment across RR	10	50	500	maximum	4.3E-03	1,000, 4E-03
0.116	S high-angle fault (1) segment to RR	10	100	1,000	minimum	5.7E-06	500, 5E-04
	See fault numbers in figure 26 as a guide.	10	250	2,500	geo mean	1.2E-04	100, 4E-06
		10	500	5,000	n	45	10, 4E-09
					std dev	7.8E-04	
					variance	6.1E-07	
					High-angle small fault*		
0.637	N high-angle fault (4)* to RR	0.01	10	0.1	maximum	7.9E-01	100, 9.6E-03
	See fault numbers in figure 26 as a guide.	0.01	50	0.5	minimum	3.1E-04	
		0.01	100	1	geo mean	1.2E-02	
		0.01	250	2.5	n	30	
		0.01	500	5	std dev	1.5E-01	
		0.1	10	1	variance	2.3E-02	
		0.1	50	5			
		0.1	100	10			
		0.1	250	25			
		0.1	500	50			

* Modeled as a small displacement Single Fracture Fault: See Caine and Forster (1999).

spread of computed K values is caused by varying gradients for any given cross-sectional area. Given the potentially large range of depth to water at the divide, the computation is relatively insensitive to gradient. The variation of K is a minimum of about one and a half orders of magnitude for the minimum to maximum gradients and for any single value of Q, and about two and a half orders of magnitude for all gradient values over the full range of Qs. In addition to relative insensitivity to gradient, the computation also is relatively insensitive to cross-sectional area, particularly when compared to the reported values of K from the bedrock-aquifer test data that span more than three orders of magnitude (fig. 25 and tables 4 and 5). Although there is a large degree of variation in the model results and data, there are two intersection zones between model results and aquifer test data that correspond to reported values of bedrock K (about 10^{-5} and about 10^{-7} m/s, table 4). The intersecting higher value (K_{max}) is, for comparison, similar to a well-sorted sand and is within the middle range for values reported for fractured crystalline rock (see Freeze and Cherry, 1979). The intersecting lower value (K_{mean}) is well within values reported for fractured crystalline rock (Freeze and Cherry, 1979). The vertical dashed green lines in figure 25 illustrate an example intersection zone formed between K_{mean} and model solutions for Q_{min}. This intersection zone corresponds to a circulation depth of approximately 250 to 390 meters below the ground surface.

Finally, note that nearly all model K values range between the values of K_{max} and K_{mean} reported from the aquifer test results (fig. 25). Thus, the model solutions indicate, given the stated simplifying assumptions and selected geometry of the models, that the bedrock alone could produce the estimated, excess ground-water discharge to the Red River surficial aquifer. As well, the K values modeled for the bedrock aquifer in combination with the suggested circulation depths could correspond to values of K and depths that are consistent with observed and reported K values for other fractured crystalline aquifer systems composed of a relatively high K weathered and fractured upper zone grading to a lower K zone at depth (Tiedeman and others, 1998; Caine and Tomusiak, 2003; Manning and others, 2004).

Computation and Results for the Caldera Margin and High-Angle Small Faults

Superimposed on the bedrock-aquifer flow system are sets of exceptionally different types of fault zones, as previously discussed (figs. 8 to 20). Assessment of the real hydraulic effects of fault zones on the flow system is hampered by the lack of any subsurface hydraulic data, such as a well that is known to penetrate one of these structures and that has

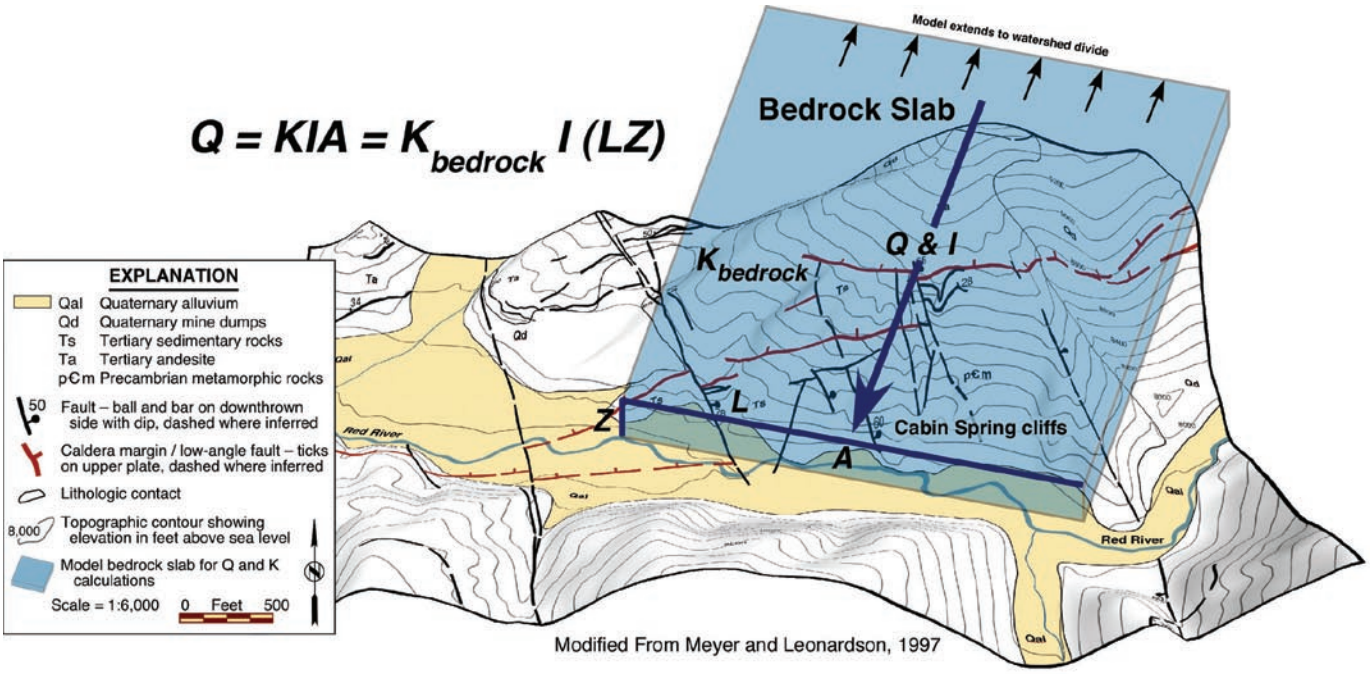

Figure 24. Pseudo three-dimensional geologic and topographic map draped on a 30-meter digital elevation model with no vertical exaggeration showing the model setup for computations of hydraulic conductivity for the bedrock aquifer system on the north divide of the Red River along the Cabin Springs inflow reach. Note that the tabular blue box is meant to represent the subsurface volume of bedrock through which the potential ground-water discharge flows and that in the computations this box extends to the northern watershed divide. Z, or depth of the cross-sectional area below the surface and through which flow occurs, is varied in the computation and L is fixed at 1,210 meters.

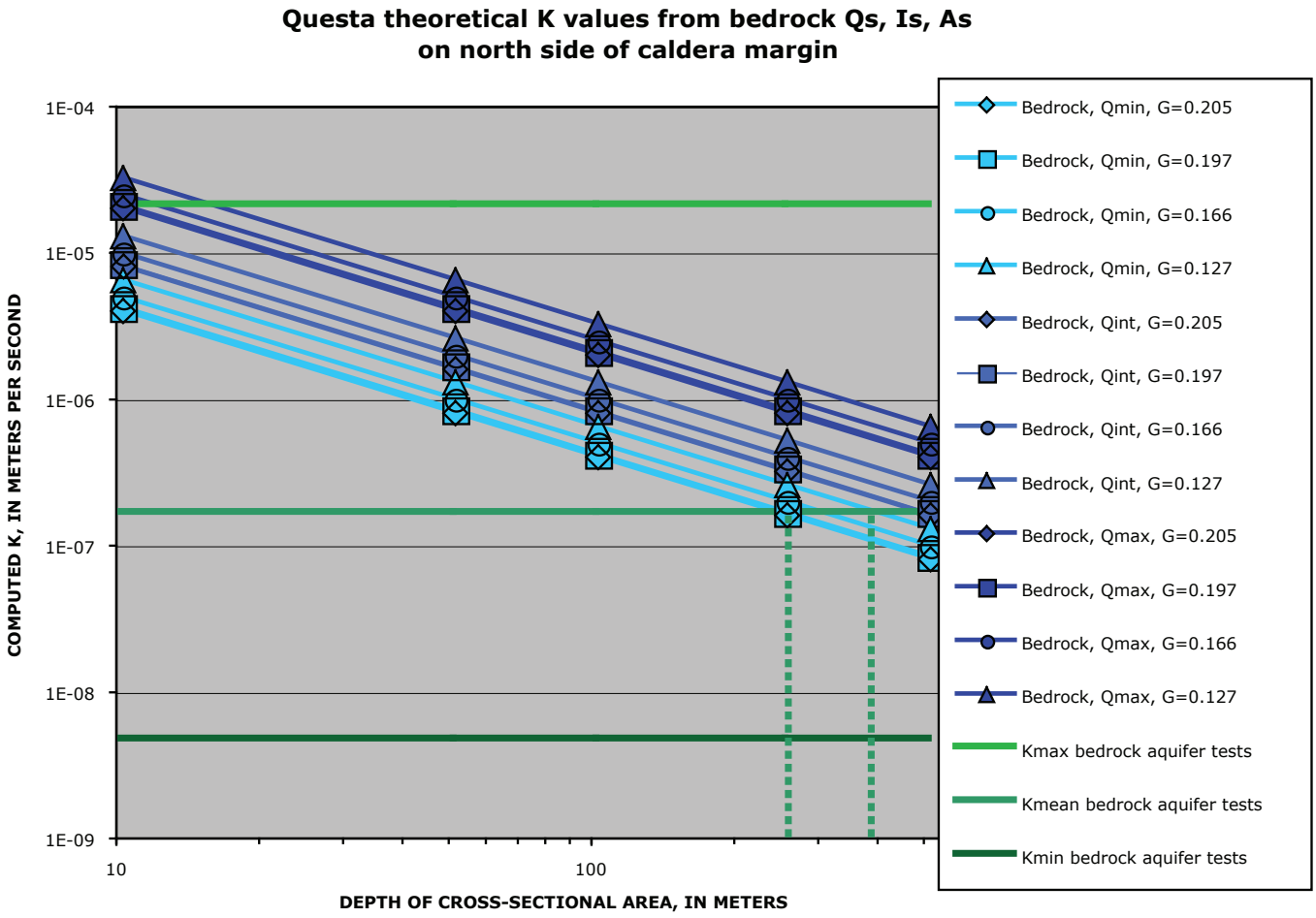

Figure 25. Plot of computed hydraulic conductivity (*K*) values relative to depth of cross-sectional areas for estimated gradients and values of estimated bedrock discharge (blue points and lines) to the Red River alluvial aquifer. Values of reported *Ks* from bedrock aquifer tests are shown as solid green lines and the dashed green lines illustrate a possible intersection solution zone where the model results are consistent with aquifer test results. *Q* = flow; *G* = gradient; min = minimum; int = intermediate; max = maximum.

carefully characterized hydraulic properties. However, the potential contributions of the structural heterogeneities relative to the bedrock alone can be estimated. This estimate can be accomplished in a way that is similar to the exercise completed for the bedrock; however, the model setup is different and is described herein.

Figure 26 shows the conceptual model for four fault zones that show geological evidence of potential intersection with the Red River surficial aquifer in the vicinity of the unaccounted-for ground-water discharge along the Cabin Springs reach and region previously modeled for the bedrock alone. Faults labeled 1 through 3 represent possible caldera margin structures with one (fault 1) on the south side of the river and two (faults 2 and 3) on the north side of the river as mapped by Meyer and Leonardson (1997) (fig. 9). Although the actual and significant hydraulic width and depth of these structures are unknown, outcrop measurements at the low-angle fault locality show an upper-plate damage zone width of about 8 to 10 meters. Fault 4 on the north side of the river represents one of the small displacement and open extensional faults (referred to herein as small faults) in the Cabin Springs cliffs (fig. 19), but the width shown in figure 26 is highly exaggerated. These are very narrow faults with widths from only a few centimeters to approximately 10 to 20 centimeters. For the computations, the width of the cross-sectional areas where they intersect the ground surface (*W*) and through which flow occurs was fixed at 10 meters for the caldera margin structures and 0.1 and 0.01 meter for the small fault (figs. 26 and 27). The subsurface extent and orientation of the faults is also poorly constrained; thus, *W* was fixed and depth (*Z*) was varied from 10 to 500 meters into the subsurface (fig. 26 and table 5). This approach results in computations for a large range of cross-sectional areas and fault-zone architectural parameters as presented in table 5. The computations also assume that the flow-source

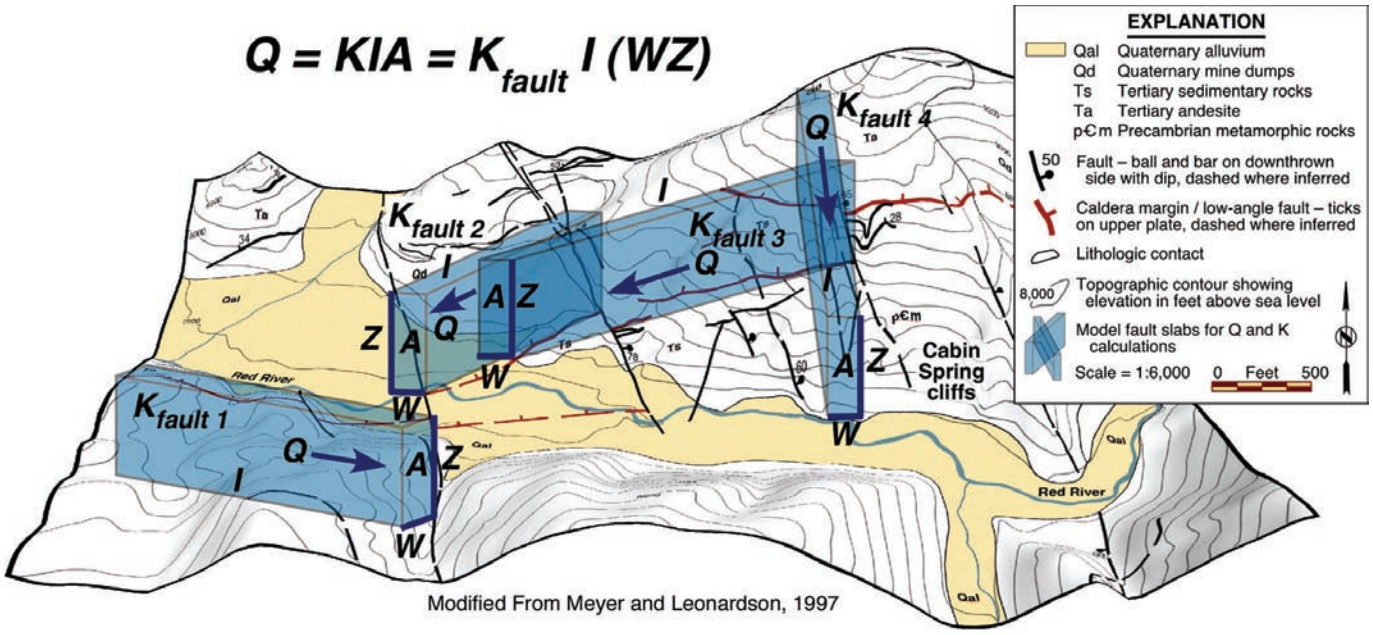

Figure 26. Pseudo three-dimensional geologic and topographic map draped on a 30-meter digital elevation model with no vertical exaggeration showing the model setup for computations of hydraulic conductivity associated with fault zones that likely intersect the Red River surficial aquifer along the Cabin Springs inflow reach. Note that tabular blue boxes are meant to represent the subsurface volume of fault zone through which potential ground-water discharge flows.

zone has an unknown extent and that ambient flow in the bedrock has no specified connection to the fault zones—the fault zones simply are flow regions of *Q* (specified by the excess inflow values of 0.01, 0.02, and 0.05 cubic meter per second as was done for the bedrock) where fault-related *K*s were computed for specified, reasonable cross-sectional areas and gradients controlled by the slope and orientation of their mapped surface traces as shown in figure 26.

Figure 27 shows the computational results for the fault zones as values of *K* plotted against depth of the damage zone or distributed deformation zone as points in lighter reds for the caldera structures and darker reds for the two small extensional fault scenarios with their associated lines. As with the bedrock, values of *K* were computed for estimated minimum, intermediate, and maximum *Q*s using equation 2 (table 5). Although there is a severe dearth of fault-related hydraulic conductivities from actual faults with architectural styles similar to those at Questa, hydraulic properties of model fault zones are reported by Caine and Forster (1999). The fault-zone models in Caine and Forster are discrete feature models constructed from field-based fault-zone architectural and fault-related fracture network data. Several of the field-based model scenarios in Caine and Forster (1999) are similar in style and size to faults at Questa, making the model results in Caine and Forster a reasonable first-order comparison. Finite-element fluid-flow simulations were run for multiple realizations of the fault-zone models to derive values of *K* for a number of model fault-zone architectural styles, fault-zone widths, and fault-related fracture-network aperture scenarios (for details see Caine and Forster [1999]). Values of *K* from Caine and Forster are thus used as a comparison to the results of the computational experiments presented here. These reported model hydraulic conductivities are shown as yellow lines of constant values of *K* in figure 27.

Like the bedrock computational results, the results for faults show a minimal relative sensitivity to the measured gradients of fault outcrop traces and circulation depths, with a higher range of computed *K*s for the caldera structures and high-angle small faults as compared with bedrock (figs. 27 and 28). Although a similar insensitivity to gradient is found for the two small extensional-fault scenarios and the caldera scenarios, it is interesting to note that the magnitude of *K*s for either small-fault scenario is one to two orders higher than for any caldera scenario, in spite of the narrowness of the small fault scenarios that are two to three orders of magnitude narrower than the caldera structures (table 5). The primary reason for this is a combination of the small-fault gradient being larger than that of any caldera margin model and in equation 2, area (*A*) is inversely proportional to *K* for given values of gradient and discharge, yet the cross-sectional areas for the small fault are one to four orders of magnitude lower than any caldera margin scenario (table 5).

In comparison, the reported model results for bulk fault zone *K* values in a number of fault zone architectural styles computed by Caine and Forster (1999) largely overlap with the range of model *K* values computed here (fig. 27). This indicates a range of plausible fault-related ground-water flow scenarios over a range of reasonable circulation depths in the

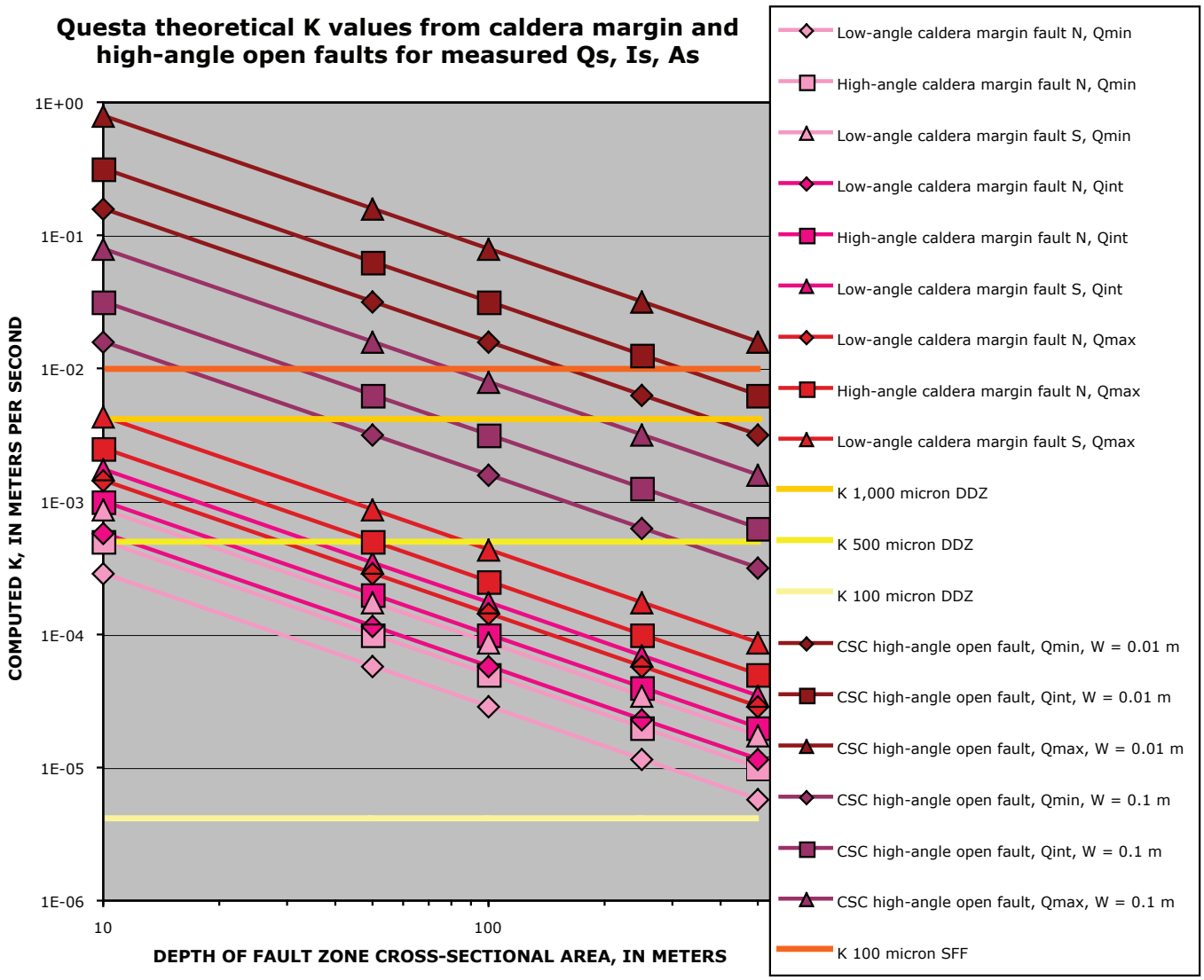

Figure 27. Plot of computed *K* values relative to depth of fault damage zones for gradients and values of estimated discharge (red points and lines) to the Red River alluvial aquifer system. Lighter reds are results for the caldera models and darker reds are for two small fault scenarios for which fault width (*W*) estimates are shown. Values of reported model *Ks* from Caine and Forster (1999) for fault zones with architectural styles similar to those found at Questa are shown as solid yellow lines for comparative purposes (see Caine and Forster, 1999). *Q* = flow; *G* = gradient; min = minimum; int = intermediate; max = maximum; N = north; S = south; CSC = Cabin Springs Cliffs; m = meters; W = width; Ang = angle; DDZ = distributed deformation zone; SFF = single fracture fault.

vicinity of Cabin Springs. Independent of bedrock flow, the caldera margin structures could produce the estimated excess flows to the Red River surficial aquifer system with conductivities that span three orders of magnitude, largely depending on the mean aperture of model fault-related and open fractures (see Caine and Forster, 1999). Figure 27 also shows a plausible scenario where a single open fracture zone with an effective hydraulic width of 0.1 meter and conductivity of about 10^{-2} m/s could produce the excess ground-water flow at Cabin Springs. Although fault-related fracture aperture may change with depth, it is likely that the effective hydraulic widths of the modeled fault zones are persistent to reasonable depths and are possibly enhanced in high-angle faults due to their subparallelism with overburden load.

As a final comparison and final important point to this exercise, figure 28 is the combination of computational results from the bedrock alone and the various fault-zone models, figures 25 and 27, respectively. Figure 28 shows that a DDZ model scenario of Caine and Forster (1999) intersects computed *K* values for Questa bedrock (yellow vertical dashed lines). The K_{max} value reported from the Questa bedrock pumping-test data also intersects caldera margin fault scenarios (figure 28, green vertical dashed lines). The important point is that although there are several plausible solutions, there is not a unique solution as to whether the bedrock alone,

one or more of the fault zone scenarios, or some combination are producing the excess ground-water inflow to the Red River alluvial aquifer.

Summary and Discussion of Potential Structural Controls on Bedrock Ground-Water Flow

The rocks exposed along the southern margin of the Questa caldera have undergone significant brittle deformation that can be characterized as structural heterogeneities that may have various potential effects on the bedrock ground-water flow system. These structures include (1) bedrock joint networks, (2) high-angle, small displacement faults, (3) the caldera-margin fault zone, (4) stockwork and other vein networks, (5) lithologic contacts, and (6) the range-front fault system. Additionally, it is important to note that the rocks at Questa reveal a unique exposure of a deeply eroded caldera system, and the extent to which the various geological structures represent other caldera fracture-dominated flow systems, particularly the caldera margin and its structural elevation, is unknown.

All joint-network properties described herein for all observed Questa bedrock lithologies indicate a system that is composed of high-intensity, highly interconnected, multiple

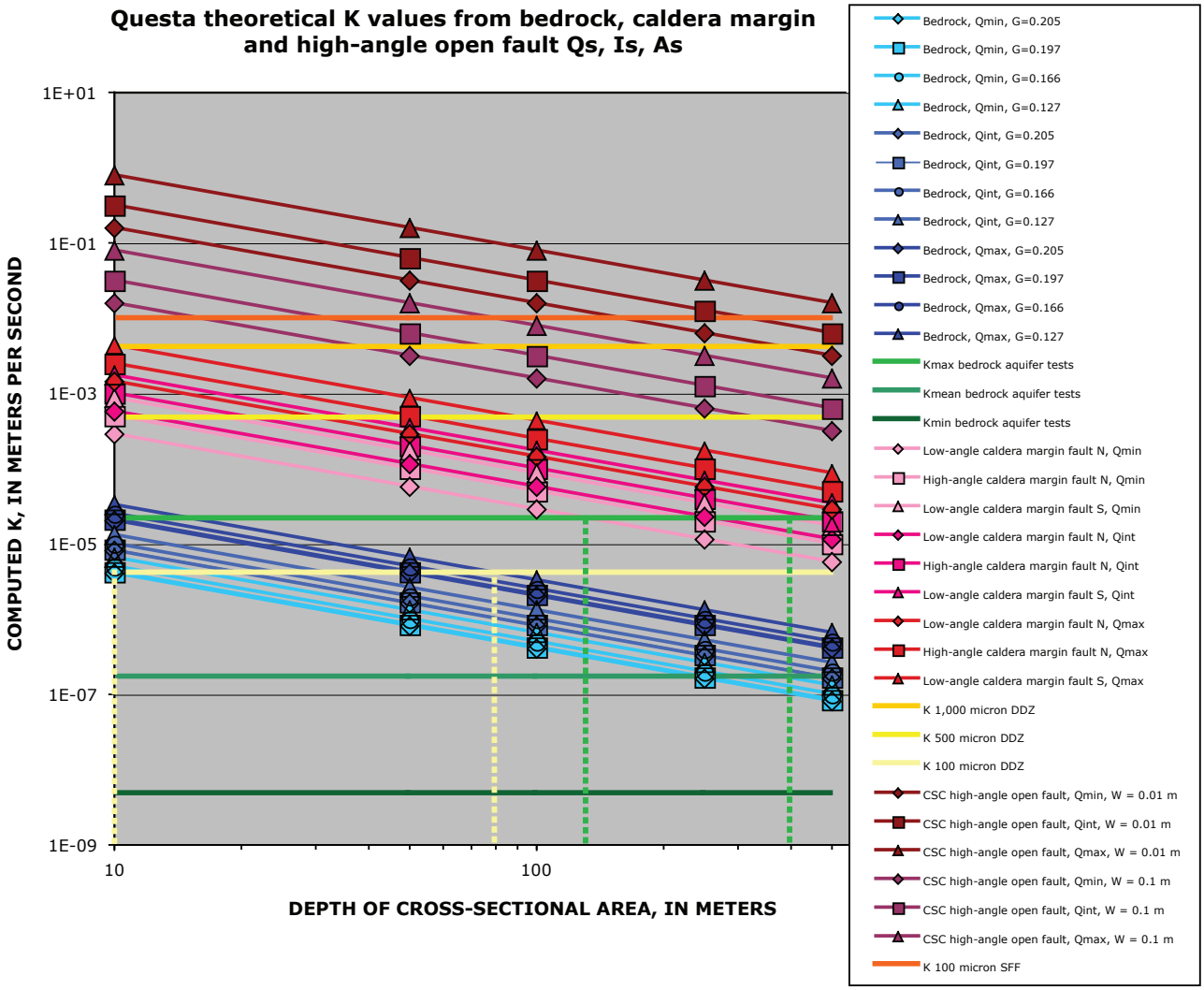

Figure 28. Combined plot (plots 25 and 27 above) of computed *K* values relative to geological feature cross-sectional area depth for the bedrock alone and for fault damage or distributed deformation zones. Note that the values of reported bedrock aquifer *K*s from Questa pumping tests and reported model *K*s from Caine and Forster (1999) shown as solid horizontal lines have overlapping intersection zones depicted as vertical dashed lines, indicating that there is not a unique solution as to which one of these geological elements is producing the estimated discharge to the Red River. *Q* = flow; G = gradient; min = minimum; int = intermediate; max = maximum; N = north; S = south; CSC = Cabin Springs Cliffs; m = meters; W = width; Ang = angle; DDZ = distributed deformation zone; SFF = single fracture fault.

orientation, generally small aperture joints. These joint networks can be thought of as the "background permeability structure" of the bedrock. This background structure may be relatively homogeneous and nearly isotropic, albeit low permeability, with respect to bulk hydraulic properties of each bedrock lithology at the well field to caldera scale (based on numerical modeling in Caine and Tomusiak, 2003, for example). These small-aperture joint networks also may provide bulk storage and geochemical reaction space from which larger aperture joints and faults obtain ground-water discharge, particularly when the aquifer is stressed. Iron oxide staining restricted to several joints in a highly connected joint network (see fig. 7) may be representative of the "plumbing," and the discrete nature of flow in general, in the shallow portion of the bedrock aquifer. Various discrete features such as an unusually wide aperture joint or open-fault zone that cut this "background permeability structure," such as those in the rhyolites outside of the ore body, may be the most important features in terms of heterogeneity and anisotropy and thus solute transport within the upper few hundred meters of the bedrock aquifer and ground-water flow system.

There are two dominant styles and orientations of major-fault zones: the low-angle, east-west-striking composite deformation zone of the caldera margin and the high-angle north-south-striking composite and distributed deformation zones, both of which cut the low-angle CDZ. The DDZs in particular show extensive internal-opening mode distributed deformation (figs. 3, 9, and 18). Within the lower Red River watershed, the topographic gradient and assumed hydraulic head gradient are toward the river, exclusive of potential local reversals of the hydraulic gradient due to mine dewatering (figs. 22 and 29). On the basis of the open nature of many of the high-angle extensional faults and the assumed potential hydraulic gradient, whether affected by mine dewatering (potential present-day case) or not (premining case), it can be inferred that there is great potential for there to be significant but highly discrete, and possibly randomly placed, north-to-south anisotropy caused by the open and crosscutting, high-angle, small extensional faults. Further, the intersections of the high-angle structures with any subhorizontal structure, whether the subhorizontal structure has a low-permeability clay-rich core or not, and particularly if they have an extensively fractured damage zone, may also cause north-to-south anisotropy in the ground-water flow system (see Caine and Forster, 1999).

The presence of brecciated iron and manganese oxide clasts in the high-angle CDZ fault-core rocks suggests an ancient, synmineralization origin for these elemental constituents. If the processes that formed this CDZ also formed the other mapped CDZs in this area (fig. 8), then these fault zones also may collectively be significant and localized, long-lived sources of bedrock-derived iron and manganese loading to bedrock ground water. Manganese dendrite surface coatings (not veins or breccias) in the fault cores of the high-angle

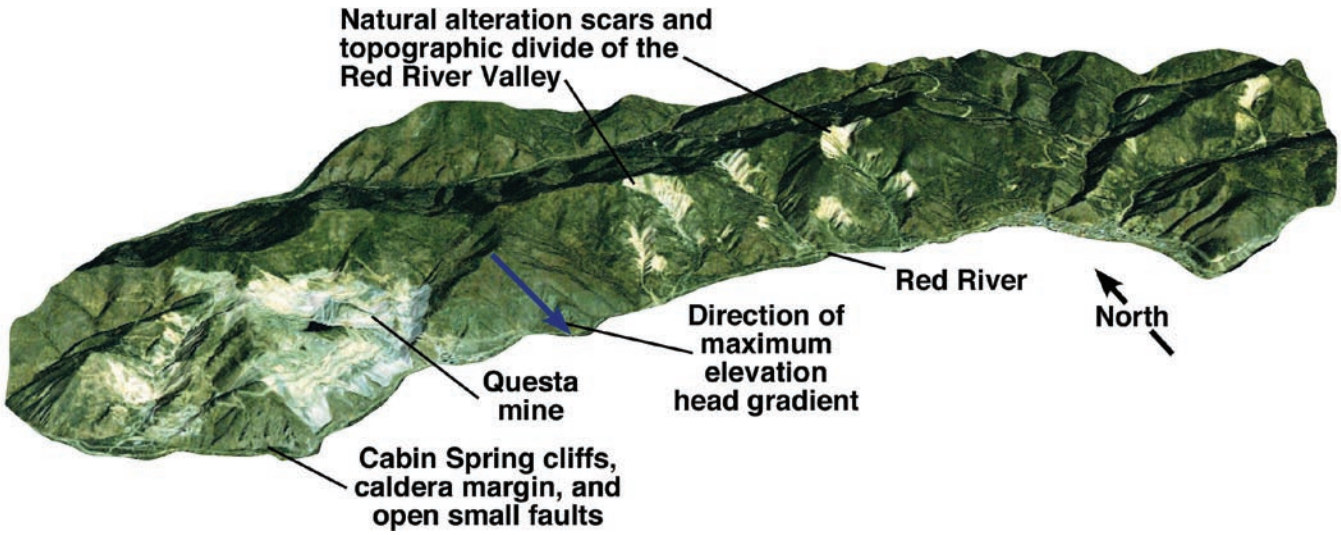

Figure 29. Fifteen-meter resolution natural color satellite image draped on a USGS digital elevation model with no vertical exaggeration. The topographic and geologic margin of the Questa caldera faces the reader. Note the extreme topographic gradient down toward the Red River; many of the high-angle extensional faults observed in the Cabin Spring cliffs area trend north-south and parallel this gradient.

DDZs below the CDZs were observed, as were manganocretes, along the banks of the Red River below these faults. This relationship attests to the high probability of long-lived, downgradient bedrock ground-water flow from the upper CDZs, through the DDZs, to discharge at the banks of the Red River, ultimately forming the manganocretes.

Although many of the fault zones in the pit ore body are filled with molybdenite, open damage-zone-related fractures may exist that are potential conductors of ground water. These structures also may be connected to the caldera margin and may be a dead end for anisotropic flow or may be a conduit that is capable of transporting mass from high levels of the ground-water flow system both vertically and laterally to lower parts of the ground-water and surface-water systems. The range-bounding fault zone may have many open brittle structures in its bedrock footwall block and relatively highly connected, combined conduit-barrier flow properties—the range-bounding fault is probably not much of a contributor to the ground-water flow system until the region near the mountain front (figs. 1 and 3). Veins are likely to be low-permeability features with respect to their host rock unless they are jointed, and the extensive stockwork vein systems may act to uniformly lower the bulk permeability of the bedrock at the well field scale where the systems exist in the subsurface. Planar vein swarms also may locally baffle or channel flow due to their presumed low permeability relative to their host rock, unless they are jointed, in which case they may cause no appreciable anisotropy.

On the basis of the descriptions of the caldera margin, the caldera margin might be a good candidate to supply bedrock ground-water discharge to the Red River. As mapped in figure 1, the caldera margin crosses the Red River in three places. When the positions of these crossings are compared with base-flow tracer-dilution study data that indicate the instream locations of surface water compared to ground-water discharges, only the crossing at Cabin Springs shows significant potential ground-water discharge to the river (McCleskey and others, 2003). The sources of such ground-water discharges are not, however, uniquely determined from the tracer study alone. For example, such discharge could come from either a high-permeability layer in substream channel alluvial materials, a zone of relatively high intensity fracturing, or a fault zone in the bedrock. The constraints on values of Q and work by Kirk Vincent (written commun., 2005) along the Cabin Springs reach represents a unique case where an unaccounted-for bedrock ground-water discharge further brings into question whether or not the caldera margin could produce this discharge or if it could be produced from the background permeability structure of the bedrock alone.

The spatial variability of the caldera-margin permeability structure is highly speculative, particularly with depth. If the low-angle fault exposure (figs. 8, 9, and 11) is a permeability structure analog for the entire caldera margin, it could have the architecture of a combined conduit-barrier. However, a number of processes could alter this permeability structure in the subsurface even if the architecture is the same as that at the surface. Of course, this structure may be different at depth and at different locations. However, if the margin is everywhere a fault zone that formed under the same conditions and processes, it could be similar to what is seen at Cabin Springs, particularly with regard to the extremely high intensity fracturing in its damage zone. Some of the processes and their possible combinations that could alter the permeability structure and hydrologic influence of the caldera margin include (1) decreased fracture aperture and closure (or opening, depending on fracture orientation as discussed herein) with depth due to overburden load (Davis and Turk, 1964; Snow, 1970 and 1972), (2) proximity of the caldera margin to fluids and mineral precipitates in them as well as various sources of heat and chemical/rock reactions capable of sealing the fault zone at depth, (3) variations in the lithologies that are cut by the margin structure and their varying responses to brittle deformation during the evolution of the zone, and (4) variations in the present-day hydrologic regime with respect to the location of the caldera margin (for example, topography and head gradients, precipitation, natural and anthropogenic discharge, and recharge).

In numerous regions throughout the United States and elsewhere, where there is low-permeability fractured crystalline bedrock underlying higher permeability surficial deposits and weathered bedrock, the bedrock is not considered a significant ground-water source (Davis and Turk, 1964; Caine and Tomusiak, 2003). Simple calculations presented here, however, show that the bedrock permeability structure alone, when treated as a continuum, could deliver inferred ground-water discharge to the Red River alluvial aquifer in the Cabin Springs reach of the Red River.

The calculations also show that if the architecture of the entire caldera margin is similar to that observed at the low-angle fault locality and if it is not sealed by mineral precipitation where it cannot be observed, the margin also could produce the significant and unaccounted-for discharge along the Cabin Springs reach. The calculations further show that an individual high-angle, open extensional fault that intersects the Red River in the vicinity of Cabin Springs and is parallel to the valley-side topographic head gradient also could produce the unaccounted-for discharge. Therefore, the calculations and all of the data available show that under the stated assumptions it is plausible that the bedrock alone, and(or) various fault zones that cut it, could produce bedrock ground-water discharge to the Red River alluvial aquifer. However, there is not a unique solution to the source of the unaccounted-for Cabin Springs ground-water discharge or probably for any similar discharges. Thus, geological observations and simple calculation are not hydraulic reality, and inferences made, such as the ones presented here, must be used with caution. Their value is that they may provide a set of testable hypotheses of what might be theoretically possible as well as geological constraints to explain certain hydraulic responses during borehole logging, other various aquifer tests, and possibly stream tracer-dilution studies.

Although there has been much work done in the Cabin Springs area, there remains a dearth of data and large uncertainties associated with understanding the bedrock flow system and its inherent structural and hydrogeological heterogeneities. Should one desire to quantify the actual permeability of a specific

volume of bedrock or geologic structure, such as the caldera margin, and its actual discharge contribution to an overlying surficial aquifer, there are several research and data-collection approaches that alone or in combination could provide greater insight. These approaches might include (1) further detailed, site-specific geological observations; (2) high-resolution seismic data acquisition; (3) drilling and coring new boreholes that are designed specifically to sample the bedrock or a discrete structure of interest that would include angled or horizontal holes if necessary; (4) detailed geophysical logging with optical and acoustic televiewers and heat pulse or electromagnetic flowmeters that would be used to identify, isolate, and sample flow specifically from the discrete bedrock zones or structures; (5) detailed, site-specific streamflow tracer-dilution and seepage studies that target specific geological features at various scales by using fault-rock geochemical, mineralogical, and paragenetic studies (for example, above and below the caldera margin where it crosses the Red River, coupled with multiple geochemical and thermal samplings of water from concurrent aquifer hydraulic testing in the well-characterized boreholes and nearby spring and seeps); and (6) dye and other tracer-injection studies utilizing the boreholes, stream, springs, and seeps. These data should also be integrated with detailed structural, petrological, geochemical, and petrophysical characterization of recovered core. Discrete interval and integrated borehole hydraulic testing coupled with water-level monitoring in well-characterized boreholes penetrating bedrock or discrete structures are likely to provide (1) important constraints on the potential contributions of bedrock ground water to acid and trace-metal loading and transport; and (2) constraints on how the bedrock might interact with surficial deposits, the open-pit mine, and underground mine workings when they are ultimately abandoned.

Acknowledgments

This work was funded by the U.S. Geological Survey, Water Resources Discipline, and done in cooperation with the New Mexico Environment Department. Other support came from the U.S. Geological Survey, Geologic Discipline, Mineral Resources Program. Permission to access the mine site was granted by MolyCorp, Inc., Questa, New Mexico. Jeff Meyer and Bruce Walker graciously showed us field localities and freely granted use of various maps and data. Reviews by Don Sweetkind and D. Kirk Nordstrom improved this manuscript as did discussions with Geoff Plumlee, Andy Manning, Philip Verplanck, and Kirk Vincent.

References Cited

Abshire, D., 1998, Report on hydrogeological connection associated with Molycorp mining activity, Questa, New Mexico: U.S. Environmental Protection Agency, Groundwater/UIC (6WQ-SG), 57 p.

Allmendinger, R.W., 1995, Stereonet—Orientation data analysis computer code: Absoft Corporation.

Barton, C.A., Zoback, M.D. and Moos, D., 1995, Fluid flow along potentially active faults in crystalline rock: Geology, v. 23, no. 6, p. 683–686.

Briggs, P.H., Sutley, S.J., and Livo, K.E., 2003, Questa baseline and pre-mining ground-water quality investigations 11—Geochemistry of alteration scars and waste piles: U.S. Geological Survey Open-File Report 2003–458, 16 p.

Caine, J.S., 2001a, The role of brittle, distributed deformation zones in the water supply of the Turkey Creek watershed fractured crystalline bedrock aquifer system, Colorado, USA: Geological Society of America and Geological Society of London, Edinburgh, Scotland, Earth System Processes Meeting, 2001 Programme with Abstracts, p. 51.

Caine, J.S., 2001b, Outcrop-based estimates of fracture porosity and permeability in crystalline rocks of the Turkey Creek watershed, Colorado Rocky Mountain Front Range, USA: Meeting proceedings of Fractured Rock 2001, Toronto, Canada, p. 148.

Caine, J.S., 2001c, Fracture network, fault zone, and geologic data collected from the Turkey Creek watershed, Colorado Rocky Mountain Front Range: U.S. Geological Survey Open-File Report 2001–416, http://geology.cr.usgs.gov/pub/open-file-reports/ofr-01-0416, 46 p.

Caine, J.S., 2003, Questa baseline and pre-mining ground-water quality investigation 6—Preliminary brittle structural geologic data, Questa mining district, southern Sangre de Cristo Mountains: U.S. Geological Survey Open-File Report 2003–280, http://pubs.usgs.gov/of/2003/ofr-03-280/, 31 p.

Caine, J.S., Evans, J.P., and Forster, C.B., 1996, Fault zone architecture and permeability structure: Geology, v. 24, p. 1025–1028.

Caine, J.S., and Forster, C.B., 1999, Fault zone architecture and fluid flow—Insights from field data and numerical modeling, *in* Haneberg, W.C., Mozley, P.S., Moore, J.C., and Goodwin, L.B., eds., Faults and sub-surface fluid flow in the shallow crust: AGU Geophysical Monograph 113, p. 101–127.

Caine J.S., and Tomusiak, S.R.A., 2003, Brittle structures and their role in controlling porosity and permeability in a complex Precambrian crystalline-rock aquifer system in the Colorado Rocky Mountain Front Range: Geological Society of America Bulletin, v. 115, p. 1410–1424.

Carpenter, R.H., 1968, Geology and ore deposits of the Questa molybdenum mine area, Taos County, New Mexico, *in* Granton-Sales, J.D., and Ridge, J.D., eds., Ore deposits of the United States, 1933–1967: American Institute of Mining Metallurgical, and Petroleum Engineers, p. 1328–1350.

Clark, K.F., 1968, Structural controls in the Red River District, New Mexico: Economic Geology, v. 63, p. 553–566.

Cowie, P.A., and Scholz, C.H., 1992, Displacement-length scaling relationship for faults—Data synthesis and discussion: Journal of Stuctural Geology, v. 14, p. 1149–1156.

Davis, S.N., and Turk, L.J., 1964, Optimum depth of wells in crystalline rocks: Ground Water, v. 2, p. 6–11.

Freeze, R.A., and Cherry, J.A., 1979, Groundwater: Englewood Cliffs, N.J., Prentice-Hall, Inc., 604 p.

Gale, V.G., and Thompson, A.J.B., 2001, Reconnaissance study of waste rock mineralogy: Questa, New Mexico, Petrography, PIMA spectral analysis and Rietveld analysis, PetraScience Consultants Inc., 31 p.

Grauch, V.J.S., and Keller, G.R., 2004, Gravity and aeromagnetic expression of tectonic and volcanic elements of the southern San Luis basin, New Mexico and Colorado, *in* Brister, B.S., Bauer, P.W., Read, A.S., and Lueth, V.W., eds., Geology of the Taos region: New Mexico Geological Society Guidebook, v. 55, p. 230–243.

GSi Water, Inc., 1996, Geohydrologic evaluation, Cabin Springs area, Red River Valley, New Mexico: GSi Water, Inc., South Pasadena, California, November, 90 p.

Hubbert, M.K., 1940, The theory of groundwater motion: Journal of Geology, v. 48, p. 785–944.

Kamb, W.B., 1959, Ice petrofabric observations from Blue Glacier, Washington, in relation to theory and experiment: Journal of Geophysical Research, v. 64, p. 1891–1909.

Kluth, C.F., and Schaftenaar, C.H., 1994, Depth and geometry of the northern Rio Grande rift in the San Luis Basin, south-central Colorado, *in* Keller, G.R., and Cather, S.M., eds., Basins of the Rio Grande rift—Structure, stratigraphy, and tectonic setting: Geological Society of America Special Paper 291, p. 27–37.

Knight, P.J., 1990, The flora of the Sangre de Cristo Mountains, New Mexico, *in* Bauer, P.W., Lucas, S.G., Mawer, C.K., and McIntosh, W.C., eds., Tectonic development of the southern Sangre de Cristo Mountains, New Mexico: New Mexico Geological Society Guidebook, v. 41, p. 94–95.

Knipe, R.J., Jones, G., and Fisher, Q.J., 1998, Faulting, fault sealing and fluid flow in hydrocarbon reservoirs—An introduction, *in* Jones, G., Fisher, Q.J., and Knipe, R.J., eds., Faulting, fault sealing, and fluid flow in hydrocarbon reservoirs: Geological Society of London Special Publication 147, p. vii–xxi.

Lipman, P.W., 1981, Volcano-tectonic setting of tertiary ore deposits, southern Rocky Mountains: Arizona Geological Society Digest, v. 14, p. 199–213.

Lipman, P.W., 1983, The Miocene Questa caldera, northern New Mexico—Relation to batholith emplacement and associated molybdenum mineralization, *in* Proceedings of the Denver Region Exploration Geologists Society symposium; the genesis of Rocky Mountain ore deposits; changes with time and tectonics: Denver Region Exploration Geologists Society, 1983, p. 133–149.

Lipman, P.W., and Reed, J.C., Jr., 1989, Geologic map of the Latir Volcanic Field and adjacent areas, northern New Mexico: U.S. Geological Survey Miscellaneous Investigations Series, Map I–1907, scale 1:48,000.

Livo, K.E., and Clark, R.N., 2002, Mapped minerals at Questa, New Mexico, using Airborne Visible-InfraRed Imaging Spectrometer (AVIRIS) data—Preliminary report: U.S. Geological Survey Open-File Report 2002–0026.

LoVetre, S.H., Nordstrom, D.K., Maest, A.S., and Naus, C.A., 2004, Questa baseline and pre-mining ground-water quality investigation 3—Historical ground-water quality for the Red River Valley, New Mexico: U.S. Geological Survey Water-Resources Investigations Report 2003–4186, 49 p.

Lucius, J.E., Bisdorf, R.J., and Abraham, J., 2001, Results of electrical surveys near Red River, New Mexico: U.S. Geological Survey Open-File Report 2001–0331, 40 p.

Ludington, S.D., Plumlee, G.S., Caine, J.S., Bove, D., Holloway, J.M., and Livo, K.E., 2004, Questa baseline and pre-mining ground-water quality investigation 10—Geologic influences on ground and surface waters in the lower Red River watershed, New Mexico: U.S. Geological Survey Scientific Investigations Report 2004–5245, 41 p.

Manning, A.H., Caine, J.S., Verplanck, P.L., Bove, D.J., and Landis, G.P., 2004, Insights into groundwater flow in an alpine watershed provided by a coupled heat, mass, and fluid transport model, Handcart Gulch, Colorado: Annual Meeting, Denver, Colorado, Geological Society of America Abstracts with Programs, 2004, v. 36, p. 539.

McCleskey, R.B., Nordstrom, D.K., Steiger, J.I., Kimball, B.A., and Verplanck, P.L., 2003, Questa baseline and pre-mining ground-water quality Investigation 2—Low-flow (2001) and snowmelt (2002) synoptic/tracer water chemistry for the Red River, New Mexico: U.S. Geological Survey Open-File Report 2003–148, 166 p.

Meyer, J.W., and Foland, K.A., 1991, Magmatic-tectonic interaction during early Rio Grande rift extension at Questa, New Mexico: Geological Society of America Bulletin, v. 103, p. 993–1006.

Meyer, J.W., and Leonardson, R.W., 1990, Tectonic, hydrothermal and geomorphic controls on alteration scar formation near Questa, New Mexico, *in* Tectonic development of the southern Sangre de Cristo Mountains, New Mexico, Guidebook: New Mexico Geological Society, v. 41, p. 417–422.

Meyer, J.W., and Leonardson, R.W., 1997, Geology of the Questa mining district—Volcanic, plutonic, tectonic and hydrothermal history: Socorro, New Mexico Bureau of Mines and Mineral Resources Open-File Report 431, 187 p.

Naus, C.A., McCleskey, R.B., Nordstrom, D.K., Donohoe, L.C., Hunt, A.G., Paillet, F.L., Morin, R.H., and Verplanck, P.L., 2005, Questa baseline and pre-mining ground-water-quality investigation 5—Well installation, water-level data, and surface- and ground-water geochemistry in the Straight Creek drainage basin, Red River Valley, New Mexico, 2001–03: U.S. Geological Survey Scientific Investigations Report 2005–5088, 228 p.

Nordstrom, D.K., McCleskey, R.B., Hunt, A.G., and Naus, C.A., 2005, Questa baseline and pre-mining ground-water quality investigation 14—Interpretation of ground-water geochemistry for wells other than those in Straight Creek, Red River Valley, Taos County, New Mexico, 2002–2003: U.S. Geological Survey Scientific Investigations Report 2004–5050, 84 p.

Powers, M.H., and Burton, B.L., 2003, Questa baseline and pre-mining ground-water quality investigation 1—Depth to bedrock determinations using shallow seismic data acquired in the Straight Creek drainage near Red River, New Mexico: U.S. Geological Survey Open-File Report 2004–1236, 18 p.

Rehrig, W.A., 1969, Fracturing and its effect on molybdenum mineralization at Questa, New Mexico: Tucson, University of Arizona, Ph.D. dissertation, 194 p.

Schilling, J.H., 1956, Geology of the Questa Molybdenum mine area, Taos County, New Mexico: State Bureau of Mines and Mineral Resources, New Mexico Institute of Mining and Technology, Campus Station, Socorro, New Mexico, Bulletin 51, 87 p.

Segall, P., and Pollard, D.D., 1983, Joint formation in granitic rock of the Sierra Nevada: Geological Society of America Bulletin, v. 94, p. 563–575.

Shipton, Z.K., and Cowie, P.A., 2001, Damage zone and slip-surface evolution over μm to km scales in high-porosity Navajo Sandstone, Utah: Journal of Structural Geology, v. 23, p. 1825–1844.

Sibson, R.H., 1994, Crustal stress, faulting, and fluid flow, *in* Parnell, J., ed., Geofluids—Origin, migration, and evolution of fluids in sedimentary basins: Special publications of the Geological Society of London, v. 78, p. 69–84.

Slifer, D.W., 1996, Red River groundwater investigation, final report: New Mexico Environment Department, Surface Water Quality Bureau, March, 26 p.

Smolka, L.R., and Tague, D.F., 1989, Intensive water quality survey of the Middle Red River, Taos County, New Mexico, September 12–October 25, 1988: New Mexico Health and Environment Department, Surveillance and Standards Section, Surface Water Quality Bureau, 87 p.

Snow, D.T., 1970, The frequency and apertures of fractures in rock: Journal of Rock Mechanics and Mineral Science, v. 7, p. 23–40.

Snow, D.T., 1972, Mountain groundwater supplies: The Mountain Geologist, v. 10, no. 1, p. 19–24.

Tiedeman, C.R., Goode, D.J., and Hsieh, P.A., 1998, Characterizing a ground water basin in a New England mountain and valley terrain: Ground Water, v. 36, p. 611–620.

U.S. Geological Survey, 2004, Daily streamflow for the Nation: USGS 08265000 Red River Near Questa, New Mexico, accessed 2002–2004 at URL http://nwis.waterdata.usgs.gov/usa/nwis/discharge

Vail Engineering, Inc., 1989, A geochemical investigation of the origin of aluminum hydroxide precipitate in the Red River, Taos County, New Mexico: Vail Engineering, Inc., Santa Fe, New Mexico.

Vail Engineering, Inc., 2000, Interim report—Analysis of acid rock drainage in the middle reach of the Red River, Taos County, New Mexico: Vail Engineering, Inc., Santa Fe, New Mexico, July 2000, 37 p.

Wells, S.G., Kelson, K.I., and Menges, C.M., 1987, Quaternary evolution of fluvial systems in the northern Rio Grande rift, New Mexico and Colorado, *in* Menges, C.M., Enzel, Yehouda, and Harrison, Bruce, eds., Quaternary tectonics, landform evolution, soil chronologies, and glacial deposits—Northern Rio Grande rift of New Mexico: Friends of the Pleistocene, Rocky Mountain Cell Guidebook, p. 55–69.

Western Regional Climate Center, 2003, Historical climate information: New Mexico Climate Summaries, Red River, New Mexico (297323). Accessed July, 17, 2003, at http://www.wrcc.dri.edu/.

USGS

By Jonathan Saul Caine—Questa Investigation 18—Brittle Structures and Their Potential Influence on Bedrock Ground-Water Flow—USGS Professional Paper 1729

ISBN 141131130-2
9 781411 311305